Received: 27 September 2023 | Revised: 11 March 2024 | Accepted: 6 May 2024

DOI: 10.1002/we.2917

WILEY

RESEARCH ARTICLE

Modeling the effect of wind speed and direction shear on utility-scale wind turbine power production

Storm A. Mata[1] | Juan José Pena Martínez[2] | Jesús Bas Quesada[2] | Felipe Palou Larrañaga[2] | Neeraj Yadav[3] | Jasvipul S. Chawla[3] | Varun Sivaram[4] | Michael F. Howland[1]

[1]Department of Civil and Environmental Engineering, Massachusetts Institute of Technology, Cambridge, Massachusetts, USA

[2]Siemens Gamesa Renewable Energy Innovation & Technology, Sarriguren, Navarra, Spain

[3]ReNew Power Private Limited, Gurugram, Haryana, India

[4]Ørsted, Washington, DC, USA

Correspondence
Michael F. Howland, Department of Civil and Environmental Engineering, Massachusetts Institute of Technology, Cambridge, MA 02139, USA.
Email: mhowland@mit.edu

Funding information
MIT Office of the Vice Chancellor; Gates Millennium Scholars Program; Chevron Corporation; National Science Foundation, Grant/Award Number: CBET 2226053; Siemens Gamesa Renewable Energy; U.S. Department of Energy, Office of Science, Office of Advanced Scientific Computing Research, Department of Energy Computational Science Graduate Fellowship, Grant/Award Number: DE-SC0023112

Abstract

Wind speed and direction variations across the rotor affect power production. As utility-scale turbines extend higher into the atmospheric boundary layer (ABL) with larger rotor diameters and hub heights, they increasingly encounter more complex wind speed and direction variations. We assess three models for power production that account for wind speed and direction shear. Two are based on actuator disc representations, and the third is a blade element representation. We also evaluate the predictions from a standard power curve model that has no knowledge of wind shear. The predictions from each model, driven by wind profile measurements from a profiling LiDAR, are compared to concurrent power measurements from an adjacent utility-scale wind turbine. In the field measurements of the utility-scale turbine, discrete combinations of speed and direction shear induce changes in power production of −19% to +34% relative to the turbine power curve for a given hub height wind speed. Positive speed shear generally corresponds to over-performance and increasing magnitudes of direction shear to greater under-performance, relative to the power curve. Overall, the blade element model produces both higher correlation and lower error relative to the other models, but its quantitative accuracy depends on induction and controller sub-models. To further assess the influence of complex, non-monotonic wind profiles, we also drive the models with best-fit power law wind speed profiles and linear wind direction profiles. These idealized inputs produce qualitative and quantitative differences in power predictions from each model, demonstrating that time-varying, non-monotonic wind shear affects wind power production.

KEYWORDS
blade element theory, equivalent wind speed, power modeling, wind shear

1 | INTRODUCTION

Mitigation of anthropogenic climate change depends on the decarbonization of carbon-intensive industries, in particular, electricity generation. The share of wind energy generation in global electricity production has grown rapidly in the preceding two decades, undergoing a factor of 35× growth in total installed capacity over that time. Concurrently, the physical dimensions of utility-scale turbines have also grown at a rapid rate. In the United States, the current average hub height (94 m) and rotor diameter (127 m) of land-based turbines are 66% and 164% larger, respectively, than those 20 years ago.[1] For off-shore turbines, the average hub height (108 m) and rotor diameter (158 m) are 15% and 24% larger, respectively, than their land-based counterparts.[2] The growth in the physical size of wind turbines has corresponded to an increase in their nameplate capacity, as well, with the average generating capacity of onshore turbines nearly tripling from around 1 MW to around 3 MW and for off-shore turbines nearly quadrupling from around 2 MW to around 9 MW.[1,2] These advances in wind energy technology portend future challenges in turbine power modeling as larger physical dimensions correspond to an increased potential for experiencing complex wind conditions that affect power production.[3]

As the size of both land-based and off-shore turbines grows, they reach farther into the atmospheric boundary layer (ABL) where they may experience more complex wind profiles.[4] In particular, a characteristic feature of ABL flows is vertical wind shear. In this study, we define speed shear as the change in the wind speed profile as a function of height and direction shear as a change in the wind direction profile with height.[5] Positive direction shear indicates veering (clockwise turning with increasing height away from the ground) and negative direction shear indicates backing (counterclockwise turning).[6] Given the presence of the surface, which limits vertical length scales, vertical wind shear tends to dominate horizontal wind shear in the ABL except in very complex terrain[7,8] and spatially heterogeneous wake interactions.[9] Therefore, this study focuses only on vertical wind shear. However, we note that the influence of horizontal wind shear may be modeled similarly to that of vertical wind shear if information about horizontal wind shear is available. Shear is important to consider in modeling turbine power production because changes in wind speed and direction alter the momentum and kinetic energy flux through the rotor.[6] Moreover, given its dependence on atmospheric characteristics such as Coriolis forces, friction, stability, and large-scale forcings, the degree of shear varies both as a function of time and geographic location.[10,11] The inherently site-specific nature of wind shear motivates the need for an accurate parametric model that incorporates its effect on wind power production, beyond assessment of empirical trends.

Several factors are known to influence the degree of shear present in the ABL. At a given location, the degree of wind shear varies in time depending on the stability in the ABL.[12,13] For instance, Van Ulden and Holtslag[14] analyzed a set of measurements of wind speed and temperature profiles in the atmosphere taken across several decades and found that the magnitude of direction shear, in particular, is strongly correlated with stratification. Further, Peña et al[15] found similar results when analyzing a set of LiDAR and meteorological mast data in which both speed and direction shear tend to be stronger during times of stable stratification than unstable or neutral stratification. Further, wind shear depends on the particular geographic location of interest. Since wind direction shear primarily manifests from Coriolis effects in the Ekman spiral, its magnitude inherently depends on latitude.[10] Lindvall and Svensson[16] found that local topography influences the degree of shear that may develop in a given location, with coastal regions generally seeing lower degrees of direction shear than inland regions. Shu et al[17] also found that in these coastal regions, winds flowing from land towards open water tend to contain larger degrees of direction shear than winds that flow from open water onto land. Finally, Wharton and Lundquist[18,19] observed that even in stably stratified flows where high direction shear would normally be expected, topography that tends to form channeled flow, such as valleys, appeared to mitigate the frequency of shear.

Given the inherently site-specific nature of wind shear and manufacturer-specific nature of wind turbine design, drawing definitive conclusions with respect to the impact of shear on turbine power production has remained elusive. Wharton and Lundquist[18,19] found that at one site, stable stratification and high shear tended to correlate with higher turbine efficiency, whereas at another site, they found the opposite to be true. Additional studies by St. Martin et al[20] and Vanderwende and Lundquist[21] found different effects of shear on power production relative to the operating regime of the turbines at their respective locations, with stable conditions generally corresponding to increased power production near rated wind speeds and decreased power production below rated wind speeds. Murphy et al[22] found similar results, indicating that direction shear occurring at wind speeds below rated had generally statistically insignificant effects on power production. They found furthermore that the degree of speed shear was only weakly correlated with changes in power production. Howland et al[23,24] found that wind speed and direction shear modify the power production of wind turbines in yaw misalignment, and proposed a blade element model to account for the observed influence. Finally, Sanchez Gomez and Lundquist[25] analyzed the effect of both speed and direction shear, and found that large direction shear and small speed shear tended to correspond to decreased power production, while large speed shear and small direction shear tended to result in greater power production. The empirical results discussed above are highly varied given the site-specific trends in wind characteristics and topography in each study. The general lack of agreement in the results across studies that consider shear in relation to turbine performance suggests a few conclusions: (1) The topography, stability, and resulting characteristic wind conditions at a given location are strongly related to the observed trends in power production, and (2) the method of analysis, as well as the specific wind profile and wind turbine characteristics considered, affect the observed trends in power production.

There have been several models proposed for turbine power production to account for variations in wind speed and direction over the turbine rotor area, however, there exists no clear consensus as to which is most accurate. In this study, we compare three parametric models that

take in arbitrary wind speed and direction profiles as inputs, and we compare their power predictions to field measurements to quantify their accuracy. Further, to identify effects of site-specific wind characteristics, as well as the general effect of complexity in wind profiles on model outputs, we drive the models with two input classes separately: (1) best-fit canonical ABL profiles in which wind speed follows a power law relationship as a function of height and direction shear is linear over the rotor, and (2) wind speed and direction observations measured by a profiling LiDAR. This analysis seeks to demonstrate the potential variation produced in the model outputs when smooth, monotonic wind profiles are assumed in place of finite time-averaged, empirical wind measurements that permit non-monotonic shear.

The organization of this study is as follows: In Section 2, we provide a description of the turbine models considered in this study, including a discussion of the inputs required for each, the mechanism by which each accounts for shear, and an overview of their numerical implementation. Section 3 provides a description of the experimental design in which the supervisory control and data acquisition (SCADA) power measurements and LiDAR wind profile measurements were recorded. This section also includes a justification of the selection of two distinct input classes used to drive the models. Section 4 includes a quantitative comparison of each of the models and their accuracy in predicting the observed SCADA power by considering both correlation and overall error. We also discuss the qualitative trends observed in power production in both the SCADA power measurements and the model predictions, for both the LiDAR wind profile inputs and the canonical ABL profile inputs. Finally, Section 5 discusses the implications of the observed results and the subsequent future research directions motivated by these findings.

2 | WIND TURBINE MODELS

The following provides a description of each of the four models included in this study, along with a brief discussion on the mechanism by which each model considers variations in wind speed and direction. Table 1 summarizes the inputs required for each model.

2.1 | Hub height wind speed model

The power available to a wind turbine is given by the kinetic energy flux through the rotor disc,[26] expressed as

$$P_{\text{Aero}} = \frac{1}{2}\rho A_d U^3, \tag{1}$$

where ρ is the density of air, A_d is the area of the rotor disc, and U is the speed of the air. Following from Equation (1), we introduce the commonly used hub height wind speed model, given by

$$P_{\text{HH}} = \frac{1}{2}\rho A_d C_P U(z_h)^3, \tag{2}$$

where C_P is the coefficient of power and z_h is the hub height for a given turbine. Equation (2) is one of two methods specified in IEC Standard 61400-12-1, which provides a standardized method for wind resource assessment across different geographic locations with different site-specific wind conditions.[27,28] A feature of Equation (2) that bears emphasizing is that it considers wind speed at only a single point ($z = z_h$). Thus,

TABLE 1 Overview of model inputs.

	Wind			Turbine	
Model	**Speed**	**Direction**	**Integrated**	**Airfoils**	**Rotor**
Hub height wind speed	$U(z_h)$	–	C_P	–	A_d
Rotor-equivalent wind speed	$U(r,\psi)$	$\Lambda(r,\psi)$	C_P	–	A_d,ζ
Rotor-equivalent power	$U(r,\psi)$	$\Lambda(r,\psi)$	C_P	–	A_d,ζ
Blade element	$U(r,\psi)$	$\Lambda(r,\psi)$	–	C_L,C_D,c,θ	A_d,B,ζ,Ω

Note: A summary of the inputs to each model. Each model takes in the rotor disc area A_d and the wind speed U at either hub height z_h or as a function of the local radial position r and azimuth angle ψ over the rotor area. The rotor-equivalent wind speed, rotor-equivalent power, and blade element models take in the wind direction Λ over the rotor area and the nacelle heading ζ. In Section 2, the wind direction and nacelle heading characterize the local wind misalignment angle $\gamma_z(r,\psi) = \Lambda(r,\psi) - \zeta$ over the rotor area. The blade element model also takes in the rotor angular velocity Ω, the number of blades B, the blade pitch angle θ, the lift and drag coefficients, C_L and C_D, and the chord length c for each blade node. The hub height, rotor-equivalent wind speed, and rotor-equivalent power models take the turbine coefficient of power C_P, integrated over the rotor area.

to be strictly accurate, Equation (2) only applies in cases of uniform inflow where wind speed and direction are constant over the rotor area (i.e., no speed or direction shear), or where the effect of wind speed and direction shear is empirically incorporated into the coefficient of power C_P, which is challenging to apply in a generalized, parametric manner. Consequently, the hub height wind speed model is functionally incapable of directly modeling the dependence of wind power production on wind shear. Therefore, the results of the hub height wind speed model serve as a benchmark against which the results for the other models considered in this study are compared.

2.2 | Rotor-equivalent wind speed (REWS) model

This section summarizes the method introduced by Wagner et al[29] to account for wind speed variations over the turbine rotor disc area and further expanded by Choukulkar et al[30] to account for wind direction variations. The form of the REWS model is similar to the hub height wind speed model in that turbine power is calculated from the kinetic energy flux through the rotor disc area. However, the REWS model samples the wind field at multiple locations over the rotor disc, thereby accounting for shear. Wagner et al[29] defined the REWS as

$$U_{eq} = \frac{1}{A_d}\sum_i U_i \cdot A_i, \tag{3}$$

where the rotor disc area is divided into a series of horizontal segments. U_i is the wind speed measured in the ith segment, and A_i is the corresponding area of that segment. In this way, U_{eq} is a weighted average of the wind speed measurements taken in each segment of the rotor. Choukulkar et al[30] subsequently expanded on Equation (3) by incorporating information about variations in direction over the rotor by computing the rotor-normal wind component with a cosine projection of the incident wind vectors. This requires computing the local wind misalignment angle over the rotor area, given by

$$\gamma_z(r,\psi) = \Lambda(r,\psi) - \zeta, \tag{4}$$

where Λ is the wind direction and ζ is the turbine nacelle heading. We express the local misalignment angle γ_z and the wind direction Λ as functions of the local radial position r measured from the rotor center and the azimuth angle ψ. The geometry is shown in Figure 1A. This change in the coordinate system is chosen for convenience in computing the area average of the normal velocity components. Whereas discretizing the

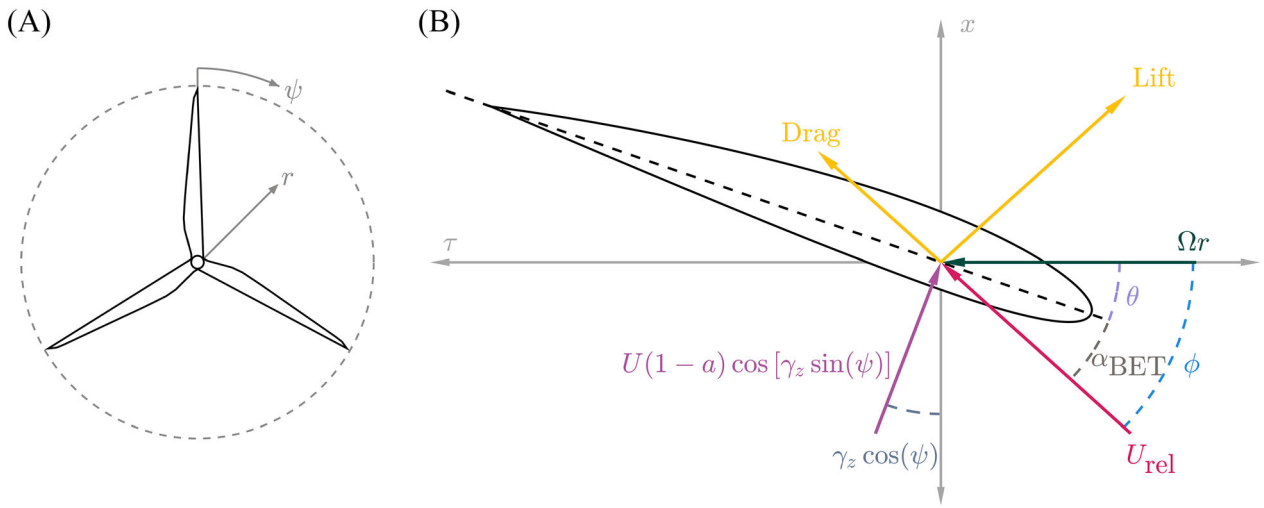

FIGURE 1 (A) Front view of a turbine rotor showing the conventions used for describing the position of the individual blade elements. The azimuth angle ψ is measured from vertical and the local radial position r from the axis of rotation. (B) A cross-sectional view of a blade element as it passes through azimuth angle $\psi = 0°$. The axial and tangential directions are represented by x and τ, respectively. The relative wind U_{rel} is computed from the axial and tangential components of the wind incident on the blade element. The axial component of the wind speed is a function of the freestream wind speed U modified by the axial induction a, the local wind misalignment angle γ_z, and the azimuth angle of the blade element ψ. The tangential component of the velocity is a function of the angular velocity Ω and the local radial position r of the blade element. The lift and drag forces are a function of the angle of attack, defined as $\alpha_{BET} = \phi - \theta$, where ϕ is the inflow angle of the relative velocity U_{rel} and θ is the local pitch angle.

rotor in Cartesian sectors requires computing the area of each individual sector, performing the integration in polar coordinates negates this step. Given this modification, the form of the REWS used in this study is given by

$$U_{\mathrm{REWS}} = \frac{1}{A_d}\int_0^{2\pi}\int_0^R U(r,\psi)\cos[\gamma_z(r,\psi)]r\,\mathrm{d}r\,\mathrm{d}\psi. \tag{5}$$

Replacing the hub height wind speed $U(z_h)$ in Equation (2) with U_{REWS} yields the REWS model, expressed as

$$P_{\mathrm{REWS}} = \frac{1}{2}\rho A_d C_P\left[\frac{1}{A_d}\int_0^{2\pi}\int_0^R U(r,\psi)\cos[\gamma_z(r,\psi)]r\,\mathrm{d}r\,\mathrm{d}\psi\right]^3. \tag{6}$$

Through simulations of turbine power production using both Equations (2) and (6), Wagner et al[29,31] found that the REWS model generally showed higher correlation with measured turbine power when input wind conditions contained large variations in speed and direction. Since it was introduced, the REWS model has been incorporated into studies on a variety of wind energy-related topics, including theoretical studies on the effect of turbulence on power production (Clack et al[32]), mesoscale modeling and wind farm parameterization (Redfern et al[33]), and further modifications to the form of the REWS model and their effect on predicted turbine power production (Murphy et al[22]).

2.3 | Rotor-equivalent power (REP) model

This section summarizes an alternative approach, also described by Wagner et al[29] and Choukulkar et al,[30] for estimating power production from arbitrary wind speed and direction inputs. Whereas Equation (6) estimates turbine power production from the kinetic energy flux produced by a rotor-average wind speed, it is likewise possible to compute the average kinetic energy flux incident on the rotor directly. To accomplish this requires a single modification to Equation (6). While the REWS model computes U_{REWS}, which is then cubed when substituted into Equation (2), the REP model moves the cube inside the area integrals, producing a single value of REWS cubed. In the REWS model, U_{REWS} replaces the $U(z_h)$ term in Equation (2), and in the REP model, the REWS cubed replaces the $U(z_h)^3$ term, yielding

$$P_{\mathrm{REP}} = \frac{1}{2}\rho C_P\int_0^{2\pi}\int_0^R [U(r,\psi)\cos[\gamma_z(r,\psi)]]^3 r\,\mathrm{d}r\,\mathrm{d}\psi. \tag{7}$$

In the formula above, we observe that if the constant terms outside the integral were moved inside, Equation (7) would produce a rotor-averaged quantity with units of power, hence the REP label applied in this study.

2.4 | Blade element (BE) model

The REWS and REP models in Equations (6) and (7) consider the rotor to be a permeable actuator disc. In these models, airfoil characteristics and the rotation of the blades are abstracted with all turbine aerodynamic information contained in the coefficient of power C_P. This representation is inherently limited in its generalizability to handle nonlinear aerodynamic interactions between the wind turbine and wind shear. BE theory is an alternative approach that explicitly considers these factors in modeling turbine power production. The following is an overview of BE theory and the process for evaluating the BE model for an arbitrary set of wind speed and direction inputs.

In a BE model of a turbine rotor, the blades are divided into discrete nodes. Because the airfoil geometry of the blades is a function of the radial position along the blade, each node will have a corresponding set of airfoil properties that govern the aerodynamics of that node. The basis of BE theory assumes (1) the forces induced on a given node may be found independently of the other elements along the blade and (2) that those forces are collectively a function of the airfoil geometry and the incident wind conditions at each element.[34,35] As the blades rotate about the center axis with inflow containing wind speed and direction variations, the wind vectors incident on each blade node are a function of the azimuthal angle ψ of each BE, as well as the radial position r of each element. Kragh and Hansen[36] introduced a method for modeling the axial forces induced on each blade node accounting for speed shear and yaw misalignment. Howland et al[23] further generalized the model to account for speed shear, direction shear, and yaw misalignment in computing the axial and tangential forces acting on each BE, along with a variable angular velocity that depends on the aerodynamic torque. This study uses the contributions of these prior works in incorporating speed and direction shear into the BE model.

What follows is a description of the sequence of calculations performed in evaluating the BE model. The process described is repeated for each element along the turbine blade. The first step in evaluating the BE model is to compute the axial and tangential components of the velocity incident on each node. Figure 1A provides a depiction of the turbine rotor and the coordinate system used in evaluating the BE model. Figure 1B shows the incident wind vectors on a blade node as it passes through the vertical position ($\psi = 0°$). The axial component of the velocity, given by

$$U_x(r,\psi) = U(r,\psi)(1-a)\cos[\gamma_z(r,\psi)\sin(\psi)]\cos[\gamma_z(r,\psi)\cos(\psi)], \tag{8}$$

is a function of the freestream velocity U modified by the axial induction a, the local wind misalignment angle γ_z, and the azimuth angle of the BE ψ. Axial induction depends on the specific induction closure model used, which we discuss in Section 2.4.1. The tangential component of the velocity is given by

$$U_\tau(r,\psi) = \Omega r - U(r,\psi)(1-a)\cos[\gamma_z(r,\psi)\sin(\psi)]\sin[\gamma_z(r,\psi)\cos(\psi)], \tag{9}$$

where Ω is the angular velocity of the rotor. Tangential induction is neglected (see Kragh and Hansen[36]). For clarity of presentation, we hereafter omit the functional dependence of U and other quantities derived from it on r and ψ. The relative velocity incident on the BE shown in Figure 1B is a function of both the axial and tangential components of the velocity and is defined by the relationship

$$U_{\text{rel}}^2 = U_x^2 + U_\tau^2. \tag{10}$$

The inflow angle of the relative velocity vector in relation to the BE is given by

$$\phi = \arctan\left[\frac{U_x}{U_\tau}\right] \tag{11}$$

and is used to compute the angle of attack on the airfoil, defined by

$$\alpha_{\text{BET}} = \phi - \theta, \tag{12}$$

where θ is the pitch angle of the BE. From the angle of attack α_{BET} (here stylized with "BET" to differentiate it from the speed shear exponent), the lift and drag coefficients (C_L and C_D, respectively) are determined for the BE. The lift and drag coefficients are typically determined empirically for a given airfoil geometry and tabulated as a function of the angle of attack. This step highlights a potential weakness in implementing the BE model. Whereas the REWS and REP models require no information about the specific aerodynamic properties of the airfoils used on a given turbine, the BE model must necessarily have this information, which may be less readily available than C_P.

The tangential force induced by the incident wind conditions on a given BE is defined by

$$\mathrm{d}f_\tau = \frac{1}{2}\rho U_{\text{rel}}^2[C_L(\alpha_{\text{BET}})\sin(\phi) - C_D(\alpha_{\text{BET}})\cos(\phi)]c\,\mathrm{d}r, \tag{13}$$

where c is the local chord length at each node. The incremental torque induced on each section by the tangential force is given by

$$\mathrm{d}Q = r\,\mathrm{d}f_\tau, \tag{14}$$

and the incremental power is then a function of the incremental torque and the rotor angular velocity, given by

$$\mathrm{d}P = \Omega\,\mathrm{d}Q. \tag{15}$$

Combining Equations (13)–(15) and integrating over the rotor area through one full rotation gives the combined rotor power, expressed as

$$P_{\text{BE}} = \frac{1}{4\pi}B\rho\Omega\int_0^{2\pi}\int_0^R U_{\text{rel}}^2[C_L(\alpha_{\text{BET}})\sin(\phi) - C_D(\alpha_{\text{BET}})\cos(\phi)]cr\,\mathrm{d}r\,\mathrm{d}\psi, \tag{16}$$

where B is the number of blades. This is the final expression for turbine power for a given arbitrary set of inflow conditions in the BE model. The influence of wind speed and direction variations on the BE model power predictions is distributed across several of the inputs listed above. The

model first accounts for shear in the calculation of the relative velocity and accompanying inflow angle, which are functions of the axial and tangential components of the wind incident on each blade node. The inflow angle is then used to determine the angle of attack, which is subsequently used to determine the lift and drag coefficients at each node, which appear explicitly in Equation (16). By this mechanism, the effect of shear on the BE model predictions cascades through the intermediate variables of the model, affecting the calculation of each subsequent variable appearing explicitly in the final equation for power in Equation (16).

2.4.1 | Induction closure and turbine controller modeling

The BE model requires that the axial induction on the rotor a and the rotor angular velocity Ω be specified, two requirements not present in the REWS and REP models. In standard blade element momentum theory, the BE equations shown in Section 2.4 are coupled with induction closure based on one-dimensional (streamwise) momentum theory: $a = (1 - \sqrt{1 - C_T})/2$, where C_T is the thrust coefficient. However, since this relationship is derived under the assumption of uniform streamwise inflow (i.e., no wind speed or direction shear), it is unclear to what extent it is valid in environments that include wind shear. Further, the rotor angular velocity is not known a priori, and it may depend on the wind speed and direction shear. In this study, we consider two candidate closures for the axial induction and three possibilities for supplying the rotor angular velocity.

For induction closure, we consider modeling frameworks where (1) axial induction is set as a constant $a = 1/3$ at the Betz limit value over the entire rotor (as in Kragh and Hansen[36] and Howland et al[23]) and (2) the axial induction is closed locally over the rotor, depending on radial and azimuthal position, based on one-dimensional momentum theory. For angular velocity, we consider: (1) the angular velocity is taken from the SCADA data, (2) the angular velocity is estimated by a controller model, and (3) the angular velocity is set to maintain a constant tip-speed ratio. We define the reference BE case as the one of greatest simplicity, with the axial induction $a = 1/3$, and Ω set to the SCADA-measured values. In the results (Section 4) for clarity of presentation, only the simple, reference BE model results are shown. The effects of the different induction and rotor angular velocity modeling choices are shown and discussed separately in Section 4.2.3.

The localized induction model is implemented as described by Madsen et al[37] In cases where the thrust coefficient exceeds a critical value of 1, momentum theory breaks down due to an inability to account for the effect of flow separation in the far wake that can cause velocities in that region to be negative.[38,39] To address this, several empirical corrections have been proposed (see, e.g., Burton et al,[40] Buhl,[41] and Madsen et al[37]). From Madsen et al,[37] a single polynomial describing the axial induction as a function of the thrust coefficient is used. The coefficients of the polynomial are chosen to best-fit standard one-dimensional momentum theory at low thrust coefficients, and to extrapolate to empirical results in high-thrust regimes. The localized induction model is given by

$$a(r,\psi) = 0.0883C_T^3(r,\psi) + 0.0586C_T^2(r,\psi) + 0.2460C_T(r,\psi), \tag{17}$$

where the axial induction is now a function of radial and azimuthal position. The local thrust coefficient is defined as

$$C_T(r,\psi) = \frac{U_{\text{rel}}^2 Bc}{U(z_h)^2 2\pi r}[C_L(\alpha_{\text{BET}})\cos(\phi) + C_D(\alpha_{\text{BET}})\sin(\phi)]. \tag{18}$$

Tip and hub loss corrections are neglected for simplicity. A sensitivity analysis (not shown for brevity) indicated that inclusion of tip and hub loss corrections affected the results on the order of <1%.

In the absence of SCADA data containing the turbine's realized tip–speed ratio, the BE model requires this information to be estimated. A common controller strategy in variable speed, pitch-regulated turbines modulates the generator torque to allow the rotor speed to vary proportionally to the inflow wind speed[40] (referred to here as the $k - \Omega^2$ model). In Region II, this model seeks to maintain a constant tip–speed ratio that theoretically maximizes power production in uniform inflow conditions. Because the turbine is tracking a fixed tip–speed ratio, the rotor speed Ω varies proportionally to the incoming wind speed. This in turn means that the torque on the rotor varies proportionally to Ω^2. The aerodynamic torque is given by

$$Q_a = \frac{1}{2}\rho\pi R^5 \frac{C_P}{\lambda^3}\Omega^2. \tag{19}$$

In steady-state operation, the controller attempts to keep the generator load torque equal to the aerodynamic torque by modulating the rotor speed. All variables on the right-hand side preceding Ω^2 are constant, and often referred to collectively as k, hence the name of this model. For implementation of this controller model, the value of k for this particular utility-scale turbine is computed by taking the slope of the line of best fit for the rotor torque as a function of the rotor angular velocity squared in the SCADA measurements. The resulting unique value of k is used to compute the rotor speed, given by

$$k\Omega^2 = \frac{P_{BE}}{\Omega}, \tag{20}$$

for all input profiles with arbitrary wind speed and direction shear, where P_{BE} is the power production estimated by the BE model given in Equation (16).

The following is a summary of the sensitivity analysis performed here. For induction closure, we consider two cases: (1) constant induction ($a = 1/3$) and (2) the momentum theory closure described in Equation (17). For the controller model, we consider three cases: (1) the angular velocity that maintains the target tip–speed ratio within the subset of Region II determined from the SCADA data (referred to hereafter as λ^*), (2) the $k - \Omega^2$ model described above, and (3) the measured angular velocity from the SCADA data. Note that because of model discrepancy, using the estimated value of k from the SCADA data does not necessarily achieve the tip–speed ratio that is targeted by the utility-scale turbine in the field setting (λ^*). We perform the sensitivity analysis with every combination of induction closure and turbine control. This scheme is designed to illustrate the influence of each model choice on the final BE model power predictions. Table 2 summarizes the six cases considered.

2.5 | Numerical implementation

Figure 2 shows illustrations of the rotor discretization schemes considered in this study. Figure 2A shows the method described by Wagner et al[29] in which the rotor is divided into a series of horizontal segments of varying area in which individual measurements of the wind field are taken. The measurements of the wind field in each horizontal segment are assumed to be constant over the segment area. The resulting REWS is then computed as the weighted average where each measurement of wind speed is weighted by the fraction of the total rotor area that its respective segment constitutes. Figure 2B shows the discretization method used for the two rotor-equivalent models in this study. We discretize the rotor into a series of concentric circles emanating from the center and draw a series of radii extending out at evenly spaced azimuth angles.

TABLE 2 Summary of the BE model sensitivity analysis setup.

Case	Induction closure	Controller model
1	Constant; $a = 1/3$	λ_{SCADA}
2	Constant; $a = 1/3$	$k - \Omega^2$
3	Constant; $a = 1/3$	Constant; $\lambda = \lambda^*$
4	Momentum theory	λ_{SCADA}
5	Momentum theory	$k - \Omega^2$
6	Momentum theory	Constant; $\lambda = \lambda^*$

Note: A description of the induction closure and controller model used in each of the six cases tested in the sensitivity analysis on the BE model.

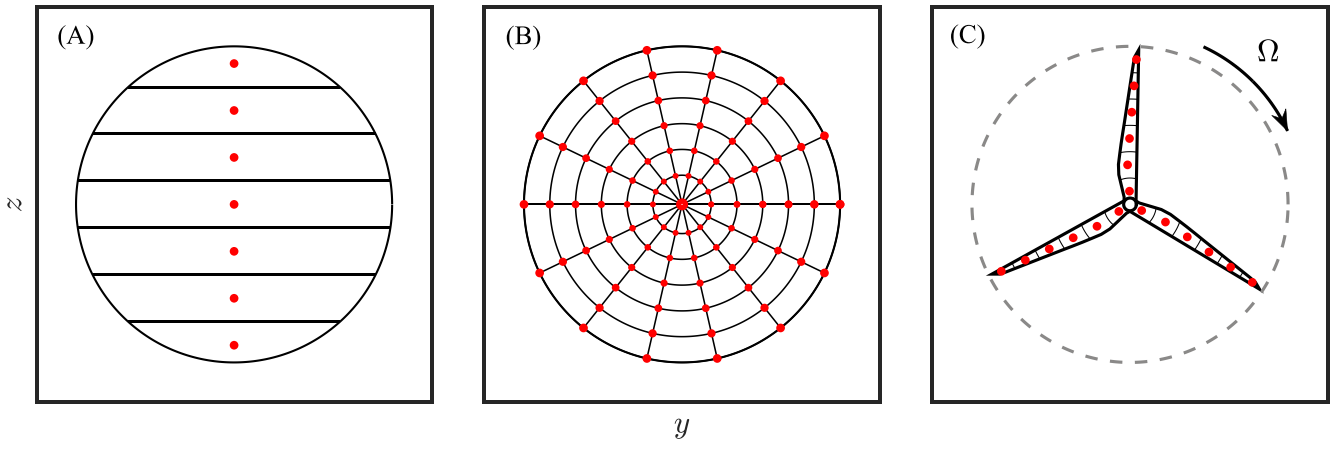

FIGURE 2 (A) Cartesian discretization of rotor disc area as described by Wagner et al[29] (B) Polar discretization used in this study for the rotor-equivalent wind speed and rotor-equivalent power models. (C) Blade element representation of the turbine rotor, showing the individual blade nodes at which the forces imparted by the wind are computed. The number of blade nodes depicted is reduced for visual clarity. Red markers in each subplot indicate the locations at which the wind field is evaluated.

The wind field is evaluated at the intersections of these annuli and radii. Figure 2C shows a representation of the BE model for the turbine rotor. As noted in Section 2.4, BE theory models the blades of the rotor and considers that they are moving through space in time, and therefore experience different degrees of wind shear as they transit a rotation of the rotor. The red markers in each subplot of Figure 2 indicate the locations at which the wind field is evaluated for each rotor discretization scheme. The models presented in Section 2 assume tilt and cone angles are zero.

The wind turbine models can be applied with instantaneous values of wind speed $U(r,\psi)$ and direction $\Lambda(r,\psi)$. However, given the inherent challenges of measuring two-dimensional instantaneous wind fields in full-scale field environments, these models are often driven by finite time-averaged wind measurements.[23,24,29,30] To account for kinetic energy contributions of turbulence in 10 min averaged wind measurements, Wagner et al[29] and Choukulkar et al[30] included turbulence intensity in their derivations of the REWS and REP models, with the turbulence intensity characterizing turbulence energetics at timescales smaller than the 10 min time-averaging scale. However, as noted by Choukulkar et al,[30] the influence of turbulence on the rotor aerodynamics (e.g., C_P, C_L, C_D) is neglected.[42] To be consistent with the shear-dependent REWS, REP, and BE formulations in the previous subsections, turbulence must be known at each position in the rotor (r,ψ). In the present field measurements, since power depends non-linearly on the instantaneous flow, we use 1 min averaged wind measurements rather than 10 min measurements.[24] Further, turbulence intensity at timescales below 1 min averaging is not available from the profiling LiDAR, but turbulence intensity is estimated at hub height ($z = z_h$) in the wind turbine SCADA data at 1 min resolution. Therefore, the models could be supplemented with the SCADA turbulence intensity, assuming a constant value over the rotor area. The effect of including the hub height turbulence intensity on the root mean square error (RMSE) of the model predictions in this study is on the order of 1%. Since this does not change the qualitative or quantitative conclusions of this study, we therefore neglect turbulence intensity in the model formulations to focus on the primary effects of wind speed and direction shear. We also neglect consideration of turbulence intensity to maintain a controlled experiment between the two rotor-equivalent models and the BE model, which does not presently incorporate information about turbulence. Future work should revisit this analysis with measurements of wind speed, direction, and turbulence kinetic energy across the rotor area in (r,ψ). Hereafter, we refer to 1 min averaged wind speed and direction measurements as $U(r,\psi)$ and $\Lambda(r,\psi)$, respectively.

3 | WIND FARM SETUP AND EXPERIMENTAL DESIGN

The wind farm in this study is located in northwestern India. The terrain at the site is primarily flat and changes in elevation by approximately 100 m over the extent of the farm, which is a distance of about 25 km. The farm contains approximately 100 utility-scale horizontal axis wind turbines from a variety of manufacturers. The hub height and rotor diameter of each turbine are both approximately 100 m.[23]

Measurements of wind velocity at the site were taken with a Vaisala Leosphere Windcube V2.0 aerosol backscatter Doppler LiDAR system. Wind speed and direction are calculated at predetermined elevations by measuring the Doppler shift in infrared light reflected off of particles in the atmosphere from successive pulses.[43] Measurements are made along four beams at a 28° angle and one vertical beam. Uncertainties in the wind speed and direction measurements are 0.1 ms^{-1} and 2°, respectively.[23,44] A total of 12 range gates from 43 m to 200 m are used, with one gate located at 104 m to make hub height measurements. Concurrent with the LiDAR measurements, power production, nacelle heading, blade pitch angle, rotor angular velocity, and other operational parameters for each turbine in the array are recorded by the onboard SCADA system. The experiment was conducted from February to April 2020. LiDAR wind profile data and SCADA turbine data are collated in 1 min averages.

The empirical results in this study use the SCADA data reported by the first turbine downstream from the LiDAR, located approximately 250 m (about two rotor diameters) away.[23] For the Region II wind speeds considered in this study, the advection timescale between the LiDAR and the turbine of interest is on the order of 20–30 s. Given the topography of the farm, we assume that the atmospheric conditions are horizontally homogeneous. While the atmosphere is seldom truly homogeneous in reality, this is a common model for the ABL provided the spatial domain is sufficiently large and flat as is the case at the site (see discussion in Stull[45] and Wyngaard[46]). While the turbine commands zero yaw misalignment, due to the time lag in the yaw controller, this does not guarantee a zero-degree yaw offset. The local wind misalignment angle defined in Equation (4) accounts for this by incorporating the turbine-measured nacelle heading rather than assuming zero yaw offset. Wind profiles in which the hub height wind speeds measured by LiDAR were outside of the inner section of Region II (6–8 ms^{-1}) were also excluded.

3.1 | Site characterization

To determine the effect of discrete combinations of speed and direction shear on turbine power production, we impose a standardized procedure to classify the degree of each type of shear observed in the LiDAR wind profile measurements. In meteorological and wind energy applications, two methods are commonly used to model wind speed as a function of height in the ABL. The first of these, the log wind profile, is a semi-empirical relationship derived from similarity theory in the surface layer, which models the wind speed as a function of the surface roughness length and surface friction velocity at a given location (see additional discussion in Lundquist[6] and Emeis and Türk[47]). Since we focus on wind shear, at least in part, above the surface layer in this study, we use the power law, defined as

$$U(z) = U_{\text{ref}}\left[\frac{z}{z_{\text{ref}}}\right]^{\alpha}, \tag{21}$$

where the speed shear exponent α is fit to each wind speed profile using least-squares regression. The reference height z_{ref} is the lowest elevation of the rotor, and the reference wind speed U_{ref} is the corresponding wind speed at that height.[6,25] The power law exponent α therefore serves as a non-dimensional quantification of the degree of speed shear in each profile. The degree of direction shear over the rotor is characterized by the average degree of turning from the bottom to the top of the rotor, given by

$$\beta = \frac{\gamma_z(z = z_h + R) - \gamma_z(z = z_h - R)}{2R}. \tag{22}$$

This method is consistent with several previous studies of direction shear in wind energy (see, e.g., Sanchez Gomez and Lundquist[25,48] and Englberger et al[49]) and in atmospheric sciences (see, e.g., Shu et al[17]), though linear fitting of the wind direction profile over the rotor area is also common (see, e.g., Brugger et al[50]). From sensitivity tests (not shown for brevity), the qualitative conclusions in this study are unaffected by the choice between Equation (22) and linear fitting methods for direction shear characterization. We follow the convention that negative direction shear ($\beta < 0^\circ\ \text{m}^{-1}$) indicates counterclockwise turning over the rotor usually referred to as backing, and positive direction shear ($\beta > 0^\circ\ \text{m}^{-1}$) indicates clockwise turning or veering.[6] For Equation (22) to be an accurate description of the wind direction variation over the rotor, the wind direction gradient must be approximately linear. To justify the assumption of linear direction shear in this study, we note (1) a review of the relevant literature for modeling the evolution of wind direction with height yields no generally accepted model (as exists for speed shear), and (2) our analysis shows that for our site, the assumption of linear direction shear is, in aggregate, more accurate than assuming no shear. In this analysis, we compute the RMSE between the LiDAR wind direction profiles and (1) profiles that contain no direction shear over the rotor area and (2) profiles that vary linearly between the wind direction at planes located at the bottom and top of the rotor. The distribution of RMSE for the model assuming no shear shows greater positive skew and a larger median RMSE (3.28°) when compared to the model assuming linear shear (1.51°). We use the above characterization of shear to qualitatively and quantitatively assess how discrete combinations of speed and direction shear affect power production observed in the empirical field measurements and in the model predictions.

Wind conditions at the site are dominated by northerly and westerly winds during the period of the experiment (see Figure 3A). Only northerly winds (330° to 45°) were retained for analysis to eliminate instances where wake effects from nearby turbines may be present in the inflow

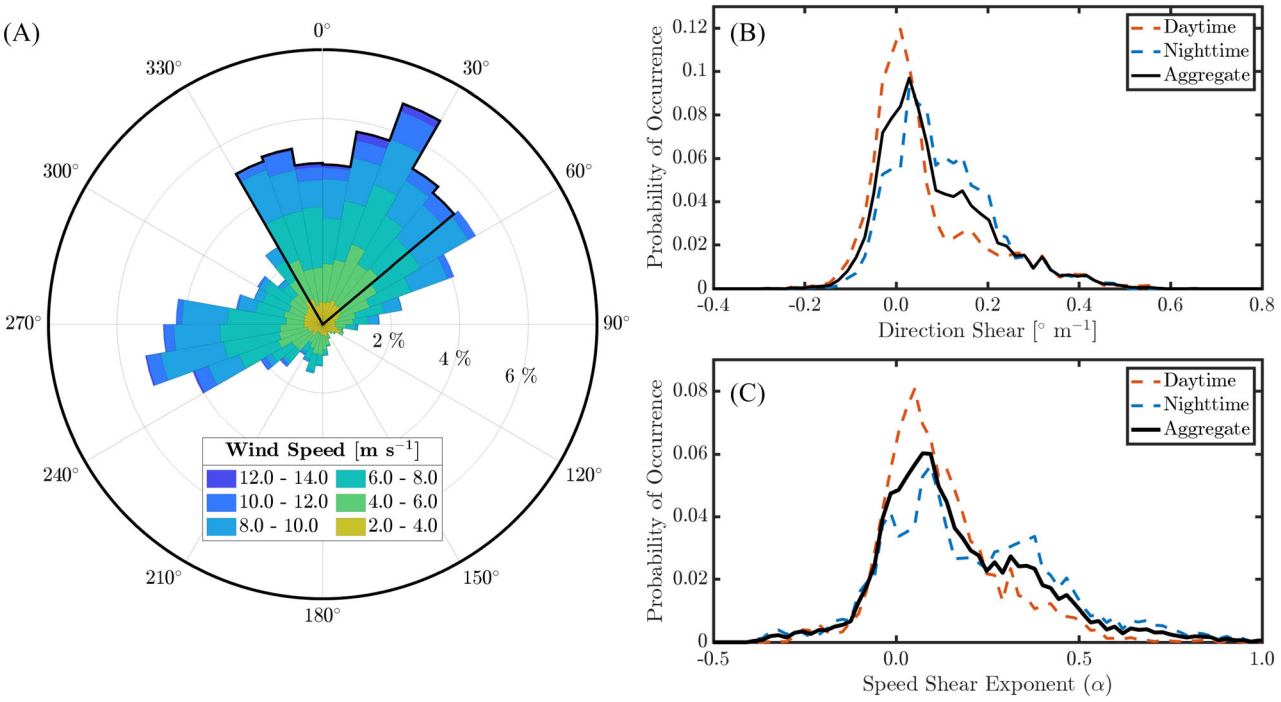

FIGURE 3 (A) Wind rose showing the distribution of hub height wind speed and direction at the site. Northerly winds inside the black border are retained for subsequent analysis, those outside are excluded to control for potential wake effects of nearby turbines. Probability distribution of the degree of (B) direction shear and (C) speed shear over the turbine rotor area. Daytime and nighttime are defined by sunrise and sunset at the site during the period of the experiment.

wind conditions. Probability distributions of speed and direction shear (see Figure 3B,C) show strong diurnal variations. Speed shear tends to be lower during the daytime hours (from sunrise to sunset), consistent with the expectation that turning is generally low in the presence of a convective boundary layer. For both daytime and nighttime, the frequency of positive speed shear is greater than that of negative speed shear. The nighttime speed shear distribution is bimodal, indicating a prevalence of shear around $\alpha = 0.2$ and $\alpha = 0.4$. We also note the presence of low-level jets (LLJs) at the site. An LLJ may occur in the stratified flows occurring at night when inertial oscillations generated by the release of turbulent stresses from the decay of the convective boundary layer align with the mean wind to form a jet near to the ground.[6] An analysis of the form described by Debnath et al[11] for systematically identifying the presence of LLJs reveals that LLJs are present in 8% of the 1 min time-averaged wind profile measurements. This analysis applied the following conditions for determining that an LLJ was present: (1) The wind speed maximum is inside the rotor area, (2) the absolute dropoff from the wind speed maximum to the local minimum above the core is $> 2 \text{ms}^{-1}$, and (3) the ratio of the dropoff to the wind speed maximum is >10%. The combination of both dimensional and non-dimensional conditions is supported by previous studies (see, e.g., Aird et al,[51] Kalverla et al,[52] and Luiz and Fiedler[53]). The complex shear profiles that can occur in the rotor area as a result of an LLJ may affect the accuracy of the power law fit in several ways. Especially large magnitudes of shear in parts of the rotor may bias the shear exponent which is based on a least-squares fit across the entire profile, indicating a higher or lower degree of shear than is present in different portions of the wind profile. Conversely, positive and negative shear occurring simultaneously over the rotor area may effectively cancel out in a least-squares fit constrained to the form of the power law profile equation. This causes the shear exponent to over-estimate shear in the negative shear region of the rotor area while simultaneously under-estimating shear in the positive shear region. This highlights a crucial deficiency with the characterization of speed shear with the power law. More generally, it is difficult to characterize wind profiles that take on many complex shapes with one or two-parameter wind profile models. This again motivates the development of an accurate parametric wind power model that can take arbitrary wind fields as input. Therefore, site and time-varying wind profiles can be provided to the power model to assess their impact on power production more broadly without requiring qualitative characterization.

Daytime direction shear is most often around $\beta = 0.0^\circ \text{ m}^{-1}$, with similar degrees of backing and veering overall. Nighttime direction shear is generally larger and more often veering than backing. Again, this could be indicative of Ekman-type flows associated with LLJs in the stable boundary layer, although we note it is not a precondition that an LLJ be present for direction shear to occur.[54]

3.2 | Wind profile model inputs

We address in Figure 4 the applicability of modeling wind speed profiles with the power law. In subplot (A), we show the power law can be an appropriate approximation of the median wind speed profile in each speed shear bin. This is possible because the non-monotonic behavior we observe in the 1 min profiles is time-varying, not always present, and at this particular site, infrequent enough to vanish in a median sense.

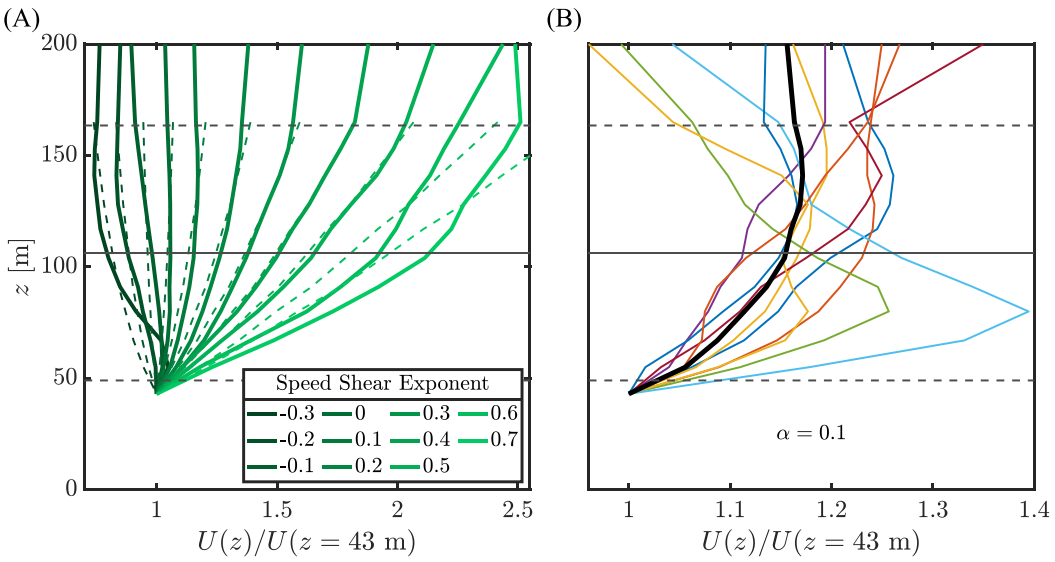

FIGURE 4 Panel (A) shows median wind speed profiles (solid lines) measured by LiDAR binned by shear exponent value and the corresponding power law profiles (dashed lines) fit to each median profile. Panel (B) shows, for the speed shear bin where $\alpha = 0.1$, the median wind speed profile in black and 10 randomly selected 1 min time-averaged wind speed profiles in color. These profiles demonstrate significant heterogeneity despite being characterized by the same speed shear exponent. The dashed grey lines indicate the top and bottom elevations of the turbine rotor. Note the horizontal scaling in (B) is modified to highlight variation in individual 1 min profiles.

Conversely, in subplot (B), we show the median wind speed profile associated with the wind speed shear bin for $\alpha = 0.1$ alongside 10 randomly selected 1 min averaged wind speed profiles that are also characterized by best-fit power laws with $\alpha = 0.1$. While the power law may be descriptive of the median profile in this case, many finite time-averaged profiles exhibit complex vertical trends, including LLJs, that are insufficiently captured by the power law with $\alpha = 0.1$.

To investigate sensitivities in the power predictions produced by the models based on deviations in the wind speed and direction profiles from their canonical representations, we test each model with two separate classes of inputs. First, each model is tested with input canonical ABL profiles where wind speed as a function of height is represented exactly by the best-fit power law relationship and wind direction shear is perfectly linear over the rotor area (see Choukulkar et al[30] and Walter[55]). Second, because these canonical models are not descriptive of the true profiles in the ABL for short time averages (as shown in Figure 4), each model is tested with the observed LiDAR wind speed and direction measurements from the profiling LiDAR. This numerical experiment will demonstrate the degree to which power predictions stemming from a power law approximation can represent the power produced by a utility-scale turbine.

3.3 | Power production normalization

Equation (1) shows that power scales as the cube of the wind speed. This relationship tends to dominate the effect of other atmospheric determinants of power, including speed and direction shear. To isolate the effect of shear on turbine power production, values of power are normalized to account for the nonlinear relationship between power and wind speed. The basis for this normalization is the median power curve, which we construct from the SCADA power measurements and their associated LiDAR wind profile measurements. SCADA power measurements are binned based on the corresponding hub height wind speed measured by LiDAR in increments of $0.5\,\mathrm{ms}^{-1}$ and the median is computed for each bin. The resulting curve, shown in Figure 5, is the median power production of the turbine, denoted by P^*, and is a function of hub height wind speed $U(z_h)$ measured by the LiDAR. Normalized SCADA power measurements and normalized model power predictions from LiDAR wind profile inputs are given by

$$\hat{P} = \frac{P}{P^*\left(U(z_h)\right)}, \tag{23}$$

where P is dimensional power and the denominator is the median power curve evaluated at the corresponding hub height wind speed for each input wind profile. Values of normalized power $\hat{P}$ relate each SCADA measurement or model prediction of power production to the median operation of the turbine across all wind conditions encountered. This procedure accounts for the cubic dependence of power on wind speed and the fact that two wind profiles with a different range of wind speed magnitudes over the rotor area may have the same degree of speed and direction shear as determined by Equations (21) and (22). Subsequent discussion of the results will reference over-performance with respect to the median power curve power production, which is defined to be values of normalized power greater than one ($\hat{P} > 1$), and under-performance, or values of normalized power less than one ($\hat{P} < 1$).

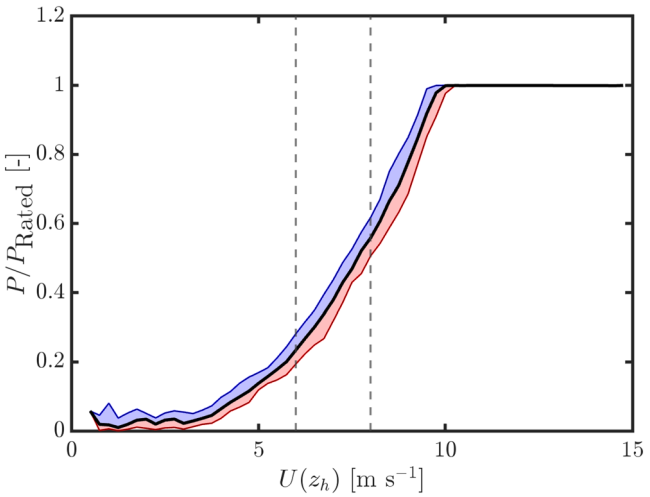

FIGURE 5 The median power curve P^* for the turbine at the site. Measurements of power from SCADA data are binned by their corresponding hub height wind speed $U(z_h)$ measured by LiDAR in increments of $0.5\,\mathrm{ms}^{-1}$. The red and blue shaded regions indicate the 25% and 75% quantiles around the median (black line). The dashed lines indicate the subset of Region II from which the LiDAR wind profiles used in this study are taken.

Following the methodology proposed by Sanchez Gomez and Lundquist[25] to assess how discrete combinations of speed and direction shear affect power production, we group empirical power measurements based on the degree of shear in their corresponding wind profiles as determined by Equations (21) and (22). We define bins of width 0.1 for α and $0.1^\circ\,\mathrm{m}^{-1}$ for β. For SCADA measurements and model predictions from LiDAR wind profile inputs, we compute the mean value of all normalized measurements of power $\hat{P}$ placed into that bin based on the degree of speed and direction shear in the input wind profiles. The resulting bin value is given by

$$\hat{P}_{\mathrm{Bin}} = \overline{\hat{P}(\beta_i, \alpha_j)}, \tag{24}$$

where $\hat{P}_{\mathrm{Bin}}$ is non-dimensional, the overbar indicates the mean across the independent 1 min averaged samples contained within the bin, and i and j are the indices for the bins along the direction shear and speed shear axes, respectively.

Conversely, for results from the canonical ABL wind profile inputs, each bin includes a single power prediction generated by the models from a single input wind profile with the specified degree of speed and direction shear. The hub height wind speed is constant in all canonical power law profiles for all combinations of speed and direction shear. Normalization by the median power curve, which accounts for different hub height wind speeds within a single bin, is not warranted. Thus, the bin value in this case is given by

$$P^{\mathrm{M}}_{\mathrm{Bin}} = P(\beta_i, \alpha_j), \tag{25}$$

where the superscript "M" in $P^{\mathrm{M}}_{\mathrm{Bin}}$ denotes that each bin contains only a single-dimensional power prediction from the models.

To assess the influence of complexities in the wind profiles not represented by the power law, we introduce a second normalization that enables a comparison between the power predictions from the simplified canonical ABL inputs and the empirical results. This second normalization addresses the fact that the bin values for empirical results ($\hat{P}_{\mathrm{Bin}}$) have been non-dimensionalized by Equation (23) while the model predictions from the canonical ABL inputs ($P^{\mathrm{M}}_{\mathrm{Bin}}$) have not. This test is intended foremost to identify the sensitivity of the model predictions to variations in the wind speed and direction profiles and deviations from their canonical ABL representations. By extension, this also demonstrates the degree of potential error that may occur in wind resource assessment performed using these models if canonical ABL profiles are assumed, provided empirically measured wind profiles are unavailable at a given site or micro-siting location. The resulting normalized empirical results and power predictions from canonical ABL profile inputs are given by

$$\tilde{P}_{\mathrm{Bin}}(\beta_i, \alpha_j) = \begin{cases} \dfrac{\hat{P}_{\mathrm{Bin}}(\beta_i, \alpha_j)}{\hat{P}_{\mathrm{Bin}}(\beta = 0^\circ\,\mathrm{m}^{-1}, \alpha = 0)} & \text{for empirical SCADA power measurements and model} \\ & \text{power predictions from LiDAR wind profile inputs,} \\ \dfrac{P^{\mathrm{M}}_{\mathrm{Bin}}(\beta_i, \alpha_j)}{P^{\mathrm{M}}_{\mathrm{Bin}}(\beta = 0^\circ\,\mathrm{m}^{-1}, \alpha = 0)} & \text{for model power predictions from canonical ABL profile inputs.} \end{cases} \tag{26}$$

This normalization relates the power predictions for all combinations of shear to the case where the inflow contains no speed or direction shear. In all figures where the normalization described in Equation (26) has been applied, the power prediction (with a normalized value of 1) in the no-shear bin has been removed to indicate that trends in power production are with respect to this bin, not the median power curve. A more detailed discussion of the differences in the model predictions between the two inputs classes and in relation to the SCADA measurements is given in Section 5.

4 | RESULTS

In the following section, we discuss the results pertaining to the two primary goals in this study. First, we discuss the trends in power production observed in the SCADA measurements when the degree of speed and direction shear present in the corresponding LiDAR wind profile measurements is characterized according to Equations (21) and (22). We then move to a discussion of the model predictions. This includes a quantitative evaluation of the correlation and overall error of the models with respect to the SCADA measurements, as well as trends in model predictions for each of the two wind profile input classes. Presented first are the model predictions when driven with the best-fit canonical ABL profile inputs, followed by the model predictions produced by LiDAR wind profile inputs. A quantitative comparison of the model predictions across the two input classes is provided. We also relate the error for each of the three models that have knowledge of variations in speed and direction over the rotor area to the hub height wind speed model, which serves as a benchmark for the other models as it does not consider shear. We end by presenting the results of the sensitivity analysis on the BE model with respect to the choice of both the induction closure and turbine controller models.

4.1 | Empirical

Figure 6 shows the effect of speed and direction shear observed in the SCADA power measurements described in Section 3.1. The values shown are the mean of all normalized power observations ($\hat{P}_{\text{Bin}}$) within each bin representing a specific combination of speed and direction shear. Only bins containing 30 or more data points are shown. Greatest over-performance to the median power curve is observed in the region bounded by $\alpha > 0.1$ and $\beta < 0.2^{\circ}\,\text{m}^{-1}$. As direction shear increases, the mean normalized power tends to decrease, with the lowest values observed in the upper right corner, corresponding to speed shear of about $\alpha = 0.3$ and direction shear of about $\beta = 0.3^{\circ}\,\text{m}^{-1}$. To demonstrate the statistical significance of the trends in over-performance and under-performance shown in Figure 6, we compute the 95% confidence interval around the mean values in each bin using bootstrapping. Bins in which the confidence interval includes the value of normalized power $\hat{P}_{\text{Bin}} = 1$ are removed from the color axis and appear as white.

The results in Figure 6 show qualitative similarities to those observed by Sanchez Gomez and Lundquist[25] in a study performed at a wind farm in central Iowa. The region of highest over-performance located in the region bounded by $\alpha > 0.1$ and $\beta < 0.2^{\circ}\,\text{m}^{-1}$ is characteristic of both sites. However, Sanchez Gomez and Lundquist did not observe wind shear falling into the region bounded by $\alpha < 0$ and $\beta > 0.3^{\circ}\,\text{m}^{-1}$, meaning that the over-performance observed in this region in Figure 6 cannot be directly compared across sites. Another notable difference in results between these two studies is the location of the greatest observed under-performance. Whereas the results in this study again show greatest under-performance in the region bounded by $\alpha > 0.1$ and $\beta > 0.1^{\circ}\,\text{m}^{-1}$, Sanchez Gomez and Lundquist observed greatest under-performance in the region bounded by $\alpha < 0.3$ and $\beta > 0.1^{\circ}\,\text{m}^{-1}$, similar to, but distinct from the results observed in this study. Several factors could influence these differences, including different rates of LLJs between the two sites, a factor which complicates analysis of these plots as noted in Section 3.1, and which will be discussed further in Section 5.

Another key difference between these studies is the time-averaging window for the LiDAR and SCADA data. This study uses 1 min time-averaged SCADA power measurements and LiDAR wind profile measurements, whereas the analysis by Sanchez Gomez and Lundquist[25] used 10 min time-averaged data. By averaging over a larger time window, the tails of the distributions for both speed and direction shear are reduced as wind profiles approach their respective median representations, as shown in Figure 4. Altering the time-averaging window may affect the trends observed by again shifting data between bins, potentially altering the mean bin value displayed, consequently changing whether those values indicate over-performance or under-performance. We therefore note that the conclusions that we draw from these plots are vulnerable to the method of shear characterization and the data processing methodology used in their generation. The utility this method presents is primarily in its ability to indicate qualitative trends in the effect of shear on power production across the range of speed and direction shear considered here, rather than predicting quantitative trends of over-performance and under-performance resulting from an input wind profile with a given combination of speed and direction shear. Quantitative predictions depending on arbitrary speed and direction shear are the focus of the modeling in Section 4.2.

4.2 | Model predictions

Given the complexity of the qualitative description of the wind profiles and of the empirical results, we investigate parametric models to predict the influence of wind shear on power production. In assessing the models, we wish to address three questions: (1) how do predictions of power vary based on the two input types used to drive the models, (2) how accurately do the models predict power based on arbitrary inflow conditions containing wind speed and direction shear from the LiDAR measurements, and (3) how accurately do the models predict power when the effect

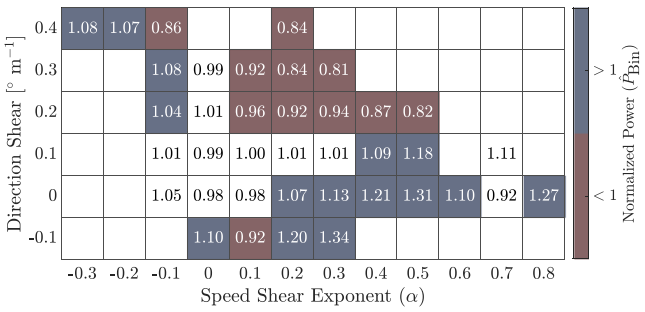

FIGURE 6 Bin averages of normalized power ($\hat{P}_{\text{Bin}}$) with respect to the median power curve of the turbine at the site for discrete combinations of speed and direction shear. Only bins containing 30 or more measurements are shown. The colormap highlights regions of over-performance and under-performance. Bins where the 95% confidence interval around the mean, as estimated by bootstrapping, includes the value $\hat{P}_{\text{Bin}} = 1$ are removed from the color axis and appear as white.

of shear is isolated from the dominant effect of the wind speed magnitude? To answer the first question, we qualitatively and quantitatively compare the predictions from the models across the two wind profile input classes. To answer the second question, we quantitatively compare the model predictions to the measured SCADA power data recorded at the same time as the LiDAR wind profiles used to drive the models. To answer the third question we develop a systematic approach to account for the fact that power scales as the cube of the wind speed. To do this, we normalize the power predictions by the kinetic energy of the inflow wind to remove the first-order effect of wind speed magnitude on power production, thereby revealing the effect of shear and other atmospheric determinants of power production. The following provides a discussion of the results of this study aimed at answering each of the three questions above.

4.2.1 | Canonical ABL profile inputs

Figure 7 shows the normalized power predictions ($\tilde{P}_{\text{Bin}}$) for the empirical data and each of the three models driven by canonical power law and linear direction shear ABL profile inputs. Each of the three models produces different qualitative and quantitative trends in predicted power over the range of speed and direction shear values considered. The REWS model (Figure 7B) predicts highest performance at the negative speed shear extreme while the REP model (Figure 7C) predicts highest performance at the positive speed shear extreme. The BE model (Figure 7D), in contrast to both REWS and REP, predicts similar levels of over-performance at both positive and negative speed shear extremes, with trends appearing to be approximately symmetric about a speed shear value of approximately $\alpha = 0.3$. We note that the BE model is driven by a constant angular velocity Ω for the canonical ABL profile inputs.

Each of the three models also shows distinctly different ranges in the spread of predicted over-performance and under-performance. The interval of predicted normalized power for each of the three models is as follows: REWS ($0.92 \le \tilde{P}_{\text{Bin}} \le 1.05$), REP ($0.93 \le \tilde{P}_{\text{Bin}} \le 1.12$), and BE ($0.96 \le \tilde{P}_{\text{Bin}} \le 1.03$). The REP model produces the highest predicted normalized power, 6.5% higher than the highest performance of the REWS model, and 8.4% higher than that of the BE model.

It is worth underscoring again that the input wind profiles corresponding to each shear bin in Figure 7B–D are identical across each of the three models. Despite this, the power predictions produced by each model show both qualitative and quantitative differences across the range of shear values tested. With respect to the two rotor-equivalent models in Figure 7B,C, the differences shown highlight the degree of discrepancy induced by computing power from the REWS and the cube of the REWS. By placing the cube of the wind speed inside the area integral in

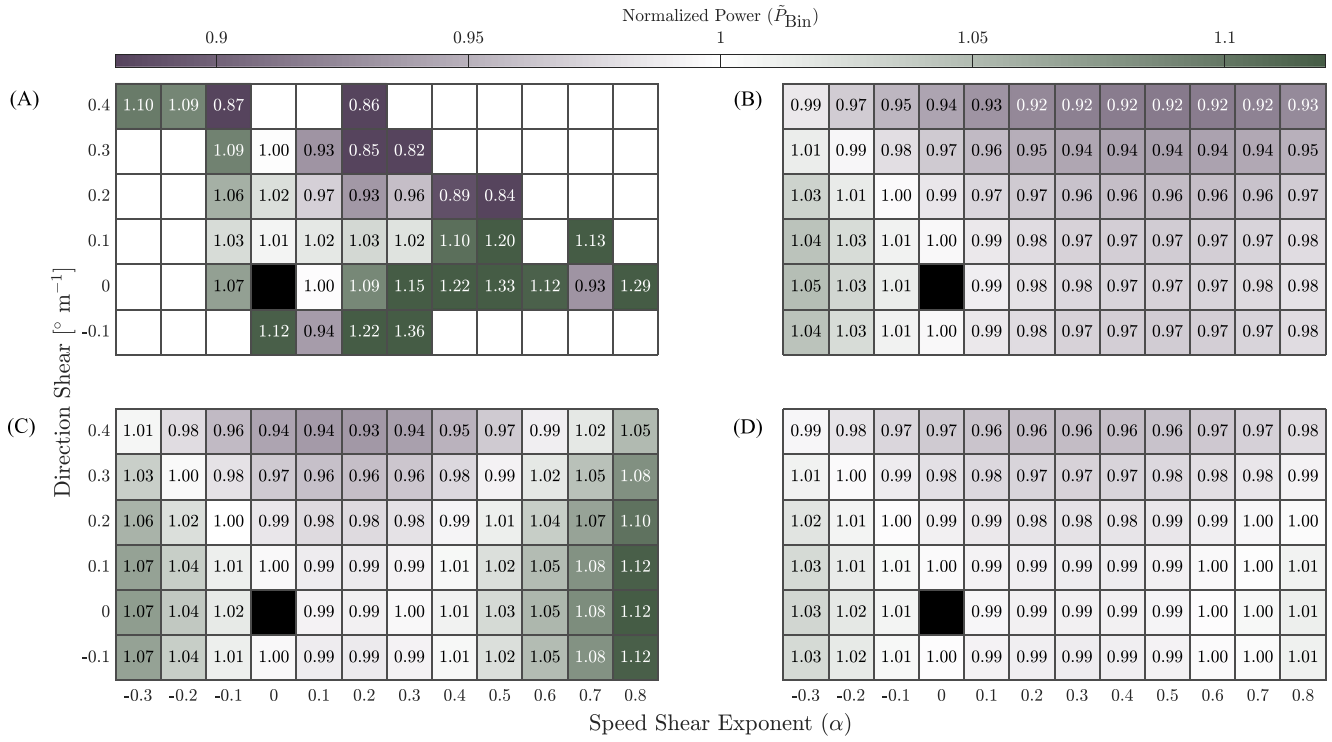

FIGURE 7 Normalized power ($\tilde{P}_{\text{Bin}}$) with respect to the square representing no speed or direction shear (indicated in black). Panel (A) shows the SCADA power measurements, (B) the REWS model, (C) the REP model, and (D) the BE model predictions from canonical ABL wind profile inputs in which wind speed is modeled with the power law and direction shear is linear over the turbine rotor area. The color axis limits are chosen to highlight trends in the model predictions presented in (B)–(D).

Equation (7), an additional region of predicted over-performance is created at the positive speed shear extreme ($\alpha = 0.8$) that the REWS model does not reflect. The BE model shows the least sensitivity to the combinations of speed and direction shear that produce the greatest predicted over-performance and under-performance in the REWS and REP models. While there are two observed areas of predicted over-performance at the extremes of the speed shear axis, similar to the REP model results, the maxima are approximately equal, and much lower in magnitude than those produced by the REP model.

In summary, the two primary results pertaining to the model predictions when driven with canonical ABL profile inputs are as follows: (1) Among the three models, despite being driven with the same profiles, the predicted power across different combinations of speed and direction shear are both qualitatively and quantitatively dissimilar, and (2) the trends in power production for each model are qualitatively and quantitatively distinct from the empirical results observed in Figure 7A. In both cases, these differences exist despite the stipulation that the degree of shear in the input wind profiles is classified in the same way (i.e., by Equations 21 and 22).

4.2.2 | LiDAR inputs

Figure 8 shows the empirical results and the model predictions for the LiDAR wind speed and direction measurement inputs. We note that the BE model results here are for Case 1 (constant induction closure of $a = 1/3$ and SCADA-measured angular velocity Ω). The BE model results for the other induction closure and controller models are shown in Section 4.2.3. As in the empirical results, only bins containing 30 or more points are shown. The trends in power are qualitatively and quantitatively distinct from those produced by the models with canonical ABL profile inputs. The smooth saddle-shape trends observed in the model outputs from canonical ABL wind profile inputs are no longer evident and the spread in predicted over-performance and under-performance has shifted for each model. The REWS model (see Figure 8B) does not show the characteristic over-performance in the region bounded by $\alpha > 0.1$ and $\beta < 0.2^\circ\,\mathrm{m}^{-1}$ as expected from the empirical results, which is present in the REP and BE models (Figure 8C,D). The 95% confidence interval was computed around the mean for each bin, as was done for the empirical results (see Figure 6). The model predictions, where bins for which the confidence interval includes $\hat{P}_{\mathrm{Bin}} = 1$ have been removed, are shown in Appendix A (see Figure A1). The interval of predicted normalized power for each of the three models with LiDAR inputs is as follows: REWS ($0.89 \le \hat{P}_{\mathrm{Bin}} \le 1.09$), REP ($0.91 \le \hat{P}_{\mathrm{Bin}} \le 1.12$), and BE ($0.87 \le \hat{P}_{\mathrm{Bin}} \le 1.10$). One of the primary findings from the results shown in Figure 8B–D is the discrepancy with the power predictions from canonical ABL wind profile inputs in Figure 7B–D. Even though the values of α and β are the same

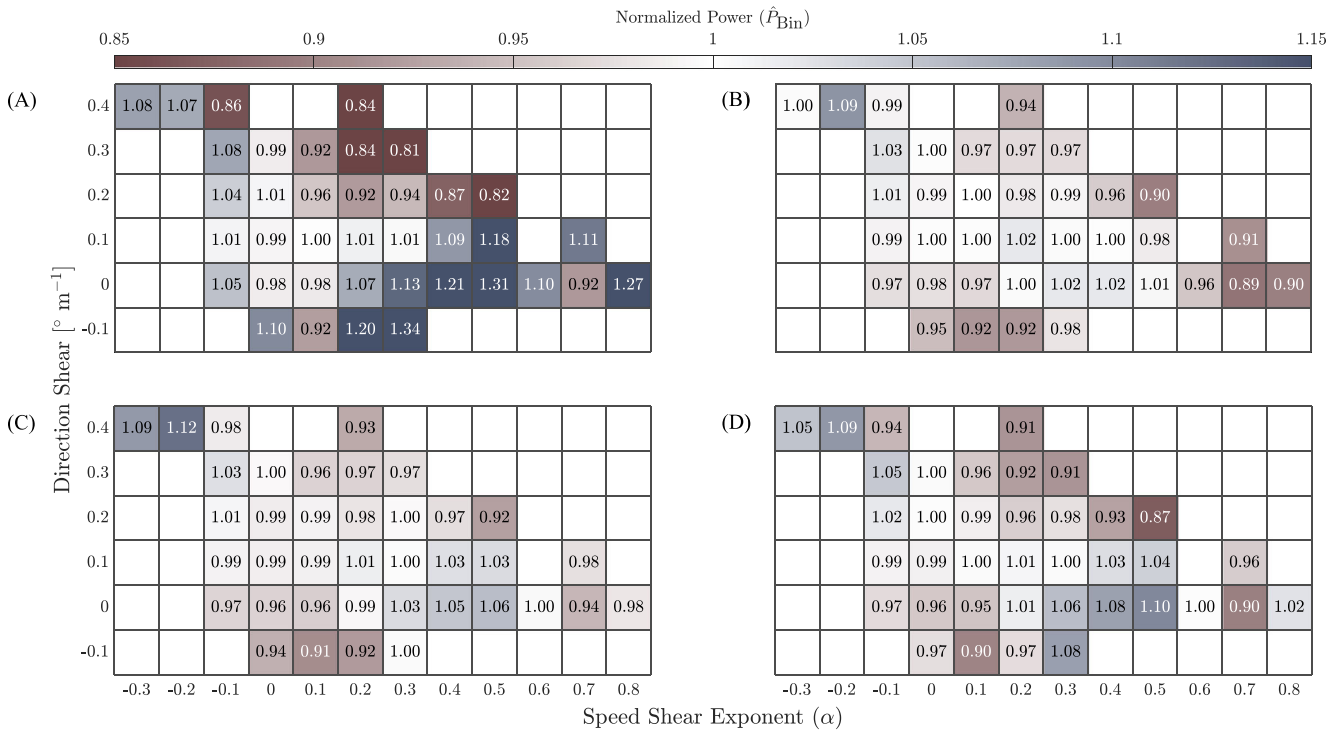

FIGURE 8 Bin averages of normalized power ($\hat{P}_{\mathrm{Bin}}$) with respect to the median power curve of the turbine at the site for discrete combinations of speed and direction shear. Panel (A) is reproduced from Figure 6 and shows the SCADA power measurements. Panel (B) shows the REWS model, (C) the REP model, and (D) the BE model predictions (Case 1) from LiDAR wind profile inputs. The colormap is chosen to highlight trends in the model predictions presented in (B)–(D).

for a given wind profile between the two input classes, the trends in predicted normalized power for each of those two inputs are inconsistent with each other across the range of shear values considered. Figure 9 shows the RMSE, defined as

$$\mathrm{RMSE}_{\mathrm{Inputs}} = \sqrt{\frac{1}{N}\sum_{i=1}^{N}\left[\frac{\hat{P}_i}{\hat{P}_{\mathrm{Bin}}(\beta=0^\circ \mathrm{m}^{-1},\alpha=0)} - \frac{P^M_{\mathrm{Bin}}}{P^M_{\mathrm{Bin}}(\beta=0^\circ \mathrm{m}^{-1},\alpha=0)}\right]^2}, \tag{27}$$

between the values in each bin for each of the three models with canonical ABL profile inputs. N is the total number of power predictions in each bin from the LiDAR inputs. Differences in the model predictions between the two input wind profile classes tend to be lowest in the region near

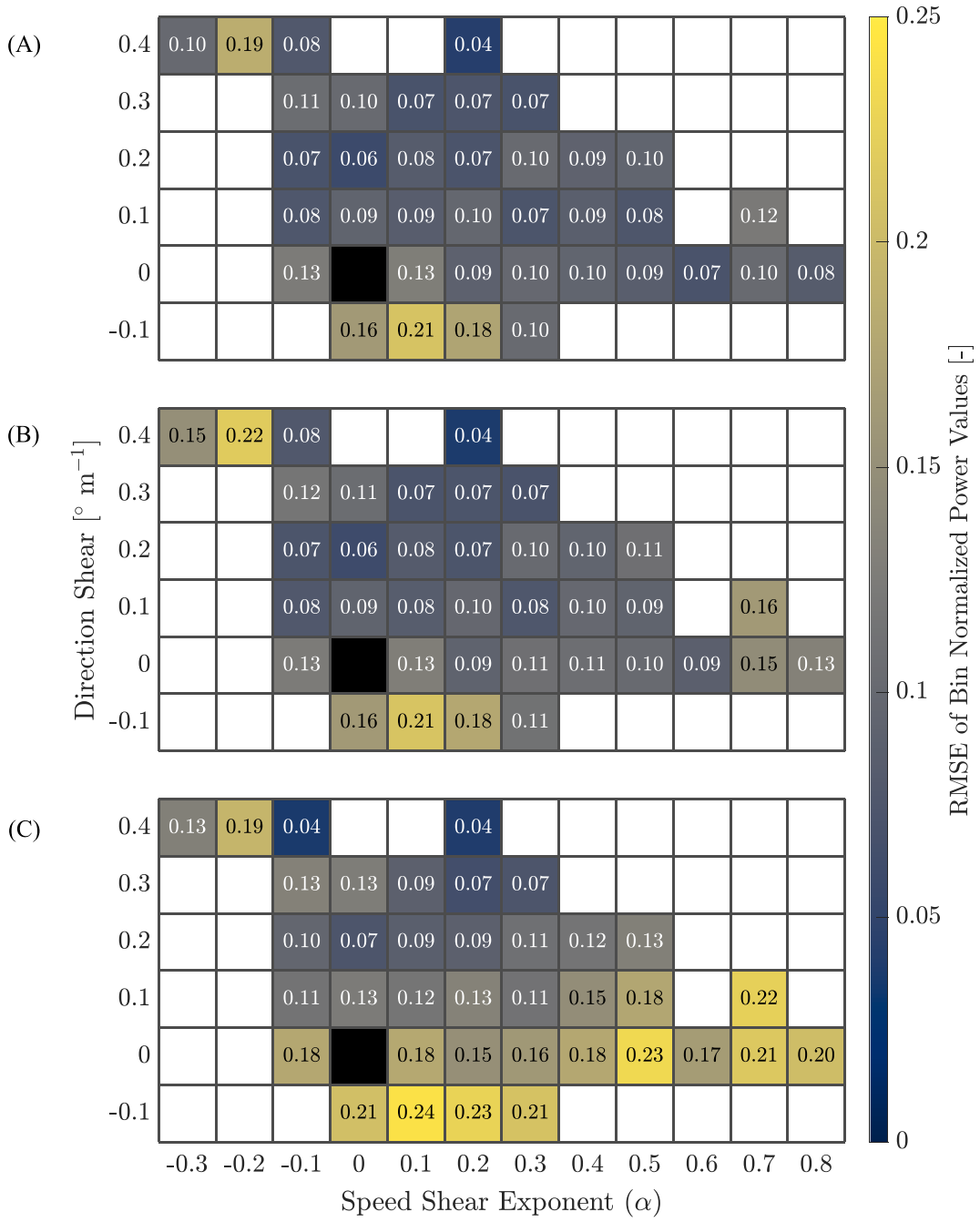

FIGURE 9 The root mean square error (RMSE) between each of the model outputs from canonical ABL wind profile inputs (see Figure 7B–D) and each of the model outputs from LiDAR wind profile inputs (see Figure 8B–D). Panel (A) shows the RMSE for the REWS model, (B) the REP model, and (C) the BE model (Case 1).

($\beta = 0.4^\circ \text{m}^{-1}, \alpha = 0.2$). The highest discrepancy occurs in the bin corresponding to $\beta = -0.1^\circ \text{m}^{-1}$ and $\alpha = 0.1$ for the REWS and BE models. The highest discrepancy occurs in the bin corresponding to $\beta = 0.4^\circ \text{m}^{-1}$ and $\alpha = -0.2$ for the REP model. The BE model has two additional regions of high discrepancy located in the area of $\beta = 0^\circ \text{m}^{-1}$ and $\alpha = 0.5$ and $\alpha = 0.7$. Maximum deviations in the model predictions between the two input wind profile classes are 0.24 for the BE model, 0.22 for the REP model, and 0.21 for the REWS model. It is notable that the largest differences between the canonical and LiDAR input profiles emerge for the BE model. Further, the BE model has the smallest spread in power for canonical inputs and the largest spread in power for the LiDAR inputs. This suggests that the BE model is more sensitive to nonlinear, non-monotonic variations in the ABL wind profiles, and also suggests the primary impact of the angular velocity Ω. Additional discussion of the variation of rotor angular velocity across different combinations of speed and direction shear, and of the effect of Ω closure on the BE model results, is provided in Section 4.2.3.

We also compare the model predictions from LiDAR inputs Figure 8B–D to the empirical data shown in Figure 8A. Similar to Equation (27), the RMSE here is defined as

$$\text{RMSE}_{\text{Empirical}} = \sqrt{\frac{1}{N}\sum_{i=1}^{N}\left(\hat{P}_{i,\text{Empirical}} - \hat{P}_{i,\text{LiDAR}}\right)^2}, \tag{28}$$

and the results are shown in Figure 10. Among the three models, bin RMSE tends to be highest when $\beta < 0.2^\circ \text{m}^{-1}$. Lowest error is observed in the region bounded by $\alpha < 0.3$ and $\beta \geq 0.2^\circ \text{m}^{-1}$. The REWS model produces the highest bin RMSE at 0.62, with the REP model following at 0.58, and finally, the BE model producing the overall lowest maximum bin RMSE at 0.51.

We show in Figure 11 the correlation between individual, 1 min averaged power production predictions for each model driven with LiDAR wind speed profiles compared to the SCADA power measurements from the utility-scale turbine described in Section 3.1. Table 3 provides a concise summary of the Pearson correlation coefficients $\mathcal{R}$ and overall RMSE for each model, as well as the performance of the models defined as the change in RMSE, $\varepsilon_{\text{RMSE}}$, relative to the hub height wind speed model, described in more detail below.

Figure 11A–D shows the correlation between model predictions and SCADA data normalized by the rated power of the turbine, a constant that does not depend on the time-varying hub height wind speed. Consequently, the model power predictions and SCADA power measurements are dominated by the cubic dependence of power on wind speed. We discuss first the performance of each model when the effect of wind speed dominates other atmospheric determinants of power, and in the next paragraph, discuss the results when the effect of shear on power production is isolated. Both the REWS and power models show similar correlations ($\mathcal{R} = 0.66$ and 0.68, respectively) and RMSE (0.245 and 0.239, respectively) with SCADA data, with the REP model having slightly higher correlation and lower error. The BE model shows the highest correlation ($\mathcal{R} = 0.86$) and lowest RMSE (0.191) among the four models. The hub height wind speed model, which has no knowledge of shear and is included as a control, shows the lowest correlation ($\mathcal{R} = 0.62$) and highest RMSE (0.253). Similarly, the BE model shows the largest reduction in RMSE relative to the hub height wind speed model, $\varepsilon_{\text{RMSE}} = -24.51\%$, in contrast to -5.53% for the REP model and -3.16% for the REWS model. While there is considerable spread between the correlations of the two rotor-equivalent model results and the BE model results, all three have lower error than the baseline hub height power model. The systematic bias in the BE model results in Figure 11D is primarily a result of the assumed rotor-constant induction and is discussed in more detail in Section 4.2.3. There is no systematic bias in the actuator disc model predictions (Figure 11B,C) because we use the coefficient of power C_P estimated directly from the empirical data. The lack of systematic bias in the actuator disc models is therefore a consequence of how the models are fit, not because of inherent knowledge of underlying physical mechanisms. If perfect knowledge of mean C_P were removed from the disc models, they would also exhibit a systematic bias.

Figure 11E–H shows the model predictions and SCADA power correlations non-dimensionalized by the aerodynamic power of the rotor computed using the hub height wind speed from each LiDAR wind speed profile, $P_{\text{Aero}} = \frac{1}{2}\rho A_d U(z_h)^3$. This controls for the cubic dependence of power on wind speed, revealing the effect of shear, among other atmospheric determinants, on power production. Notably, the correlation between the two actuator disc model predictions and the SCADA data significantly decreases when the models do not have the benefit of the cubic dependence of power on wind speed. The REWS and REP models again show similar correlations ($\mathcal{R} = 0.30$ and 0.34, respectively) and RMSE (0.123 and 0.120, respectively). The REP model again produces slightly higher correlation and lower error. Unlike the two rotor-equivalent models, the BE model correlation remains relatively high ($\mathcal{R} = 0.84$) when the cubic dependence of power on wind speed is normalized out, and the RMSE remains the lowest among the models (0.093). Again, the BE model produces the largest reduction in RMSE relative to the hub height wind speed model ($\varepsilon_{\text{RMSE}} = -26.19\%$), as compared to the two rotor-equivalent models ($\varepsilon_{\text{RMSE}} = -2.38\%$ and -4.76%). As confirmation of the theory used to justify the normalization scheme in this analysis, the predictions of the hub height wind speed model in Figure 11E are noted to have collapsed to a flat line with no correlation to the SCADA measurements. Because this model has no knowledge of variations in wind speed and direction, when normalized by P_{Aero}, the predictions should form a line along the value of C_P. This indicates that the results given for the other models in Figure 11F–H show the effect of shear on power separated from the cubic dependence of power on wind speed. The results demonstrate that while the REWS and REP models show qualitative differences in their predictions of power based on the inflow shear (the REP model has improved qualitative representation of the dependence of power on wind shear compared to REWS as shown in Figure 8), it is challenging to

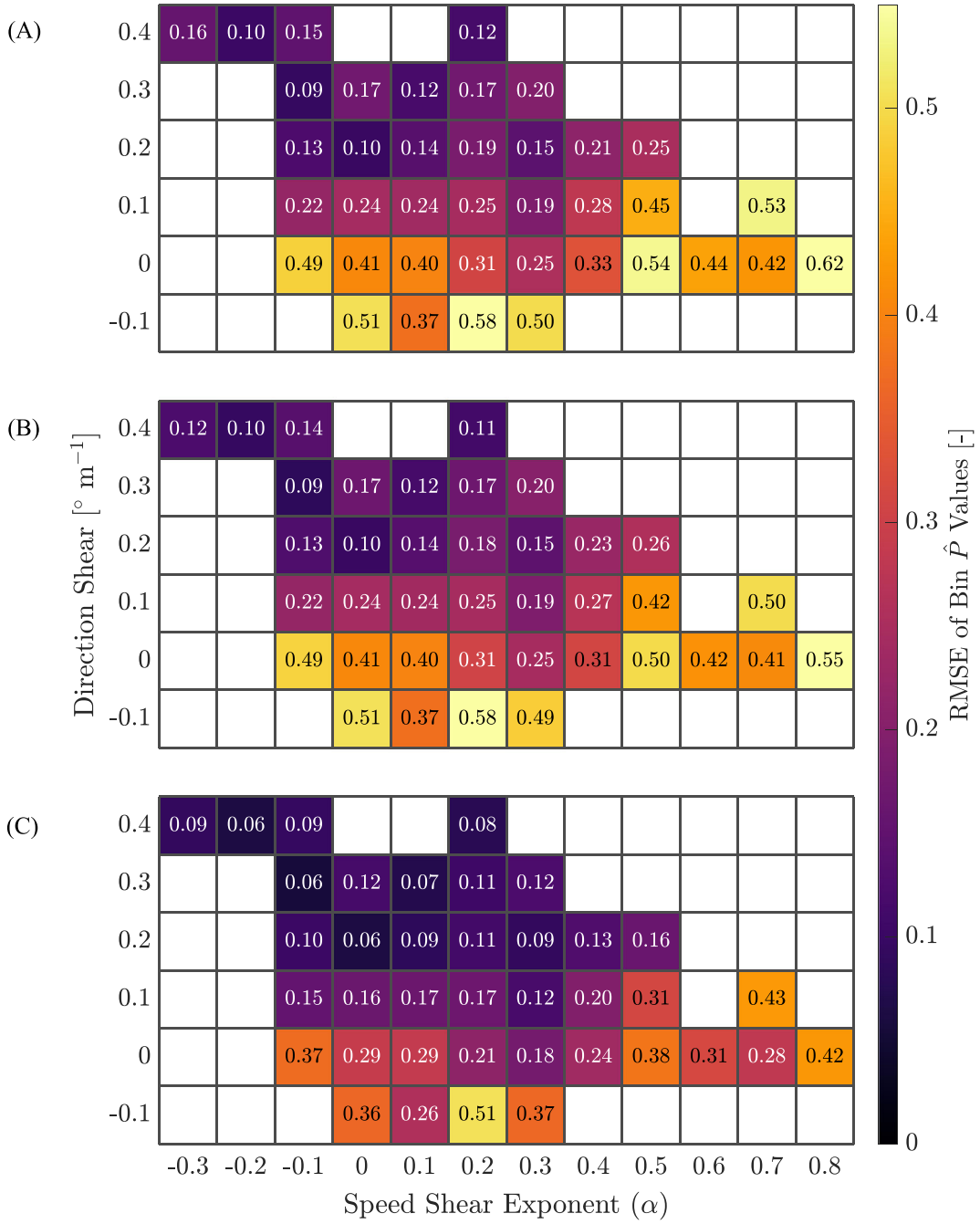

FIGURE 10 The root mean square error (RMSE) between the empirical values of normalized power (see Figure 8A) and each of the model outputs from LiDAR wind profile inputs (see Figure 8B–D). Panel (A) shows the RMSE for the REWS model, (B) the REP model, and (C) the BE model (Case 1).

elucidate which actuator disc model representation is more quantitatively accurate in the present study. Further, these results show that with respect to the overarching goal of this study to specifically model the effect of wind speed and direction shear on turbine power production, the BE model demonstrates a quantitative advantage over the two rotor-equivalent models.

4.2.3 | Influence of induction closure and controller modeling on BE model results

In this section, we provide the results of the sensitivity analysis on the BE model discussed in Section 2.4.1. Figure 12 shows the correlation between the BE model predictions and SCADA data in the same fashion as Figure 11, for each of the six cases in the sensitivity analysis (two choices for induction closure and three choices for the angular velocity closure yielding six total models). The reference case (Case 1) discussed in

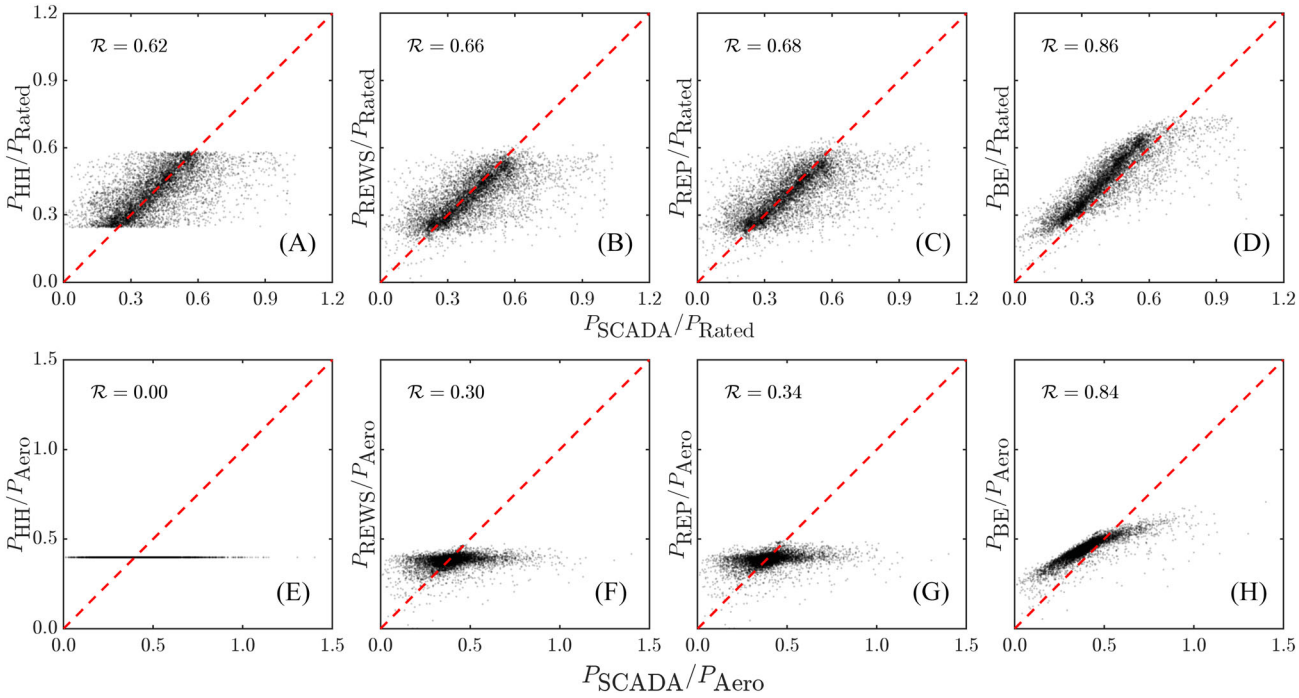

FIGURE 11 Correlation plots for each of the four models against SCADA power. The top row, A–D, shows power predictions normalized by the rated power of the turbine P/P_{Rated} and illustrates the performance of the models when the cubic dependence of power on wind speed dominates other atmospheric determinants of power. The bottom row, E–H, shows power predictions normalized by the aerodynamic power of the rotor where the wind speed is measured at hub height, $P_{Aero} = \frac{1}{2}\rho A_d U(z_h)^3$, and illustrates the performance of the models when the effect of shear and other atmospheric determinants of power are isolated. The Pearson correlation coefficient $\mathcal{R}$ is shown for each case.

TABLE 3 Summary of model correlation and overall error.

	P/P_{Rated}			P/P_{Aero}		
Model	$\mathcal{R}$	**RMSE**	ε_{RMSE} **(%)**	$\mathcal{R}$	**RMSE**	ε_{RMSE} **(%)**
Hub height wind speed	0.62	0.253	–	0.00	0.126	–
Rotor-equivalent wind speed	0.66	0.245	−3.16	0.30	0.123	−2.38
Rotor-equivalent power	0.68	0.239	−5.53	0.34	0.120	−4.76
Blade element (Case 1)	0.86	0.191	−24.51	0.84	0.093	−26.19

Note: A summary of the model correlations and errors relative to measured SCADA power production. The column labeled P/P_{Rated} shows the model performance when the cubic dependence of power on wind speed dominates other atmospheric determinants of power. The column labeled P/P_{Aero} shows the model performance when the cubic dependence of power on wind speed is removed by normalizing by the aerodynamic power of the rotor using the hub height wind speed, $P_{Aero} = \frac{1}{2}\rho A_d U(z_h)^3$. For both cases, the Pearson correlation coefficient $\mathcal{R}$, the root mean square error (RMSE), and the percent change in RMSE relative to the hub height wind speed model ε_{RMSE} are shown.

Section 4.2.2 where induction is constant and the tip–speed ratio is taken from SCADA data shows the lowest overall error and highest correlation with the empirical data. Among the five remaining cases, Case 3 ($a = 1/3; \lambda^*$) demonstrates the lowest overall error, with an increase in RMSE relative to the hub height wind speed model of 2.77% when wind speed dominates predictions of power and 1.59% when the effect of shear is isolated. Case 6 (a from momentum theory; λ^*) shows the overall highest error and lowest correlation, with an increase in RMSE relative to the hub height wind speed model of 34.78% when wind speed dominates predictions of power and 29.37% when the effect of shear is isolated. The systematic bias of the BE model predictions in Figures 11 and 12 is dependent primarily on the assumed rotor-constant induction. It remains an open question as to how induction varies as a function of speed and direction shear incident on the rotor. Since we focus in this study on how shear affects power production relative to median performance, we assume $a = 1/3$ based on the Betz limit (see additional discussion in Section 2.4.1). In a sensitivity analysis (not shown), we find that induction values greater than $a = 1/3$ decrease the bias and lower values increase the bias. In Cases 1–3 of the BE model sensitivity analysis, we hold induction constant and vary only the turbine controller model. Figure 12A–C shows the results of these tests and demonstrates that bias is also a function of the angular velocity, though the effect in this study is secondary to that of the induction. The full results of the sensitivity analysis are provided in Table 4.

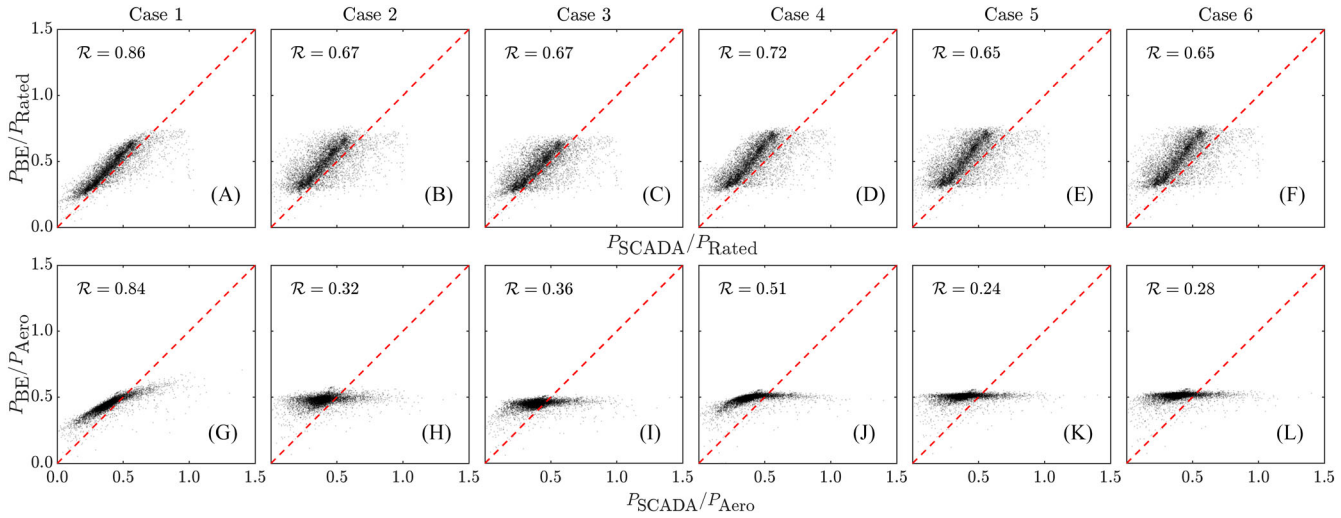

FIGURE 12 Correlation plots for each of the six sensitivity analysis cases. The top row, (A)–(F), shows power predictions normalized by the rated power of the turbine P/P_{Rated} and illustrates the performance of the models when the cubic dependence of power on wind speed dominates other atmospheric determinants of power. The bottom row, (G)–(L), shows power predictions normalized by the aerodynamic power of the rotor where the wind speed is measured at hub height, $P_{\text{Aero}} = \frac{1}{2}\rho A_d U(z_h)^3$, and illustrates the performance of the models when the effect of shear and other atmospheric determinants of power is isolated. The Pearson correlation coefficient $\mathcal{R}$ is shown for each case.

TABLE 4 Summary of correlation and overall error in the BE model sensitivity analysis.

	P/P_{Rated}			P/P_{Aero}		
BE model setup	$\mathcal{R}$	**RMSE**	$\varepsilon_{\text{RMSE}}$ **(%)**	$\mathcal{R}$	**RMSE**	$\varepsilon_{\text{RMSE}}$ **(%)**
Case 1 ($a = 1/3; \lambda_{\text{SCADA}}$)	0.86	0.191	−24.51	0.84	0.093	−26.19
Case 2 ($a = 1/3; k - \Omega^2$)	0.67	0.294	+16.21	0.32	0.143	+13.49
Case 3 ($a = 1/3; \lambda^*$)	0.67	0.260	+2.77	0.36	0.128	+1.59
Case 4 (mom. theory; λ_{SCADA})	0.72	0.297	+17.39	0.51	0.143	+13.49
Case 5 (mom. theory; $k - \Omega^2$)	0.65	0.336	+32.81	0.24	0.160	+26.98
Case 6 (mom. theory; λ^*)	0.65	0.341	+34.78	0.28	0.163	+29.37

Note: A summary of the BE model correlations and errors relative to measured SCADA power production. The column labeled P/P_{Rated} shows the model performance when the cubic dependence of power on wind speed dominates other atmospheric determinants of power. The column labeled P/P_{Aero} shows the model performance when the effect of shear and other atmospheric determinants of power is isolated through normalization by the aerodynamic power of the rotor using the hub height wind speed, $P_{\text{Aero}} = \frac{1}{2}\rho A_d U(z_h)^3$. For both cases, the Pearson correlation coefficient $\mathcal{R}$, the root mean square error (RMSE), and the percent change in RMSE relative to the hub height wind speed model $\varepsilon_{\text{RMSE}}$ are shown.

In Figure 13, we compare the trends in predicted power production between the best performing setup (Case 1, which uses Ω from the SCADA data), and the best performing setup in which Ω is modeled (Case 3). Overall, using the value of Ω corresponding to λ^* rather than Ω from the SCADA measurements reduces the spread in the maximum degree of predicted over-performance and under-performance. Furthermore, in several bins (e.g., ($\beta = 0.4^\circ \text{m}^{-1}, \alpha = -0.1$) and ($\beta = 0.3^\circ \text{m}^{-1}, \alpha = 0.2$)), predicted under-performance when the BE model is driven with SCADA Ω becomes predicted over-performance when driven with a constant tip–speed ratio. This comparison, where all other factors are constant between the two cases, demonstrates the degree to which the BE model predictions are dependent on the rotor angular velocity Ω closure.

In Figure 14, we analyze the ability of the $k - \Omega^2$ model in Case 2 to predict the realized tip–speed ratio. Subplot (A) shows the mean bin value for the realized tip–speed ratio from the SCADA data normalized by the target value commanded by the turbine controller (λ^*). Subplot (B) shows the mean bin value for the predicted tip–speed ratio from the controller model in Case 2. Subplots (C) and (D) show the same data in (A) and (B), respectively, normalized by the mean value of the bin corresponding to no speed or direction shear. There exist distinct trends in the SCADA data (Figure 14A) between above-target tip–speed ratios ($\lambda > \lambda^*$) and over-performance ($\hat{P}_{\text{Bin}} > 1$) in Figure 6. While there does appear to be some degree of correlation in the model predictions (most noticeable in subplot (D) where normalized λ values less than 1 generally coincide with under-performance in Figure 6, these trends are less pronounced. There also exists less spread in the variation of predicted normalized tip–speed ratios (0.97 to 1.02 in Figure 14D) as compared to the SCADA measurements (0.94 to 1.11 in Figure 14C). We also observe that the $k - \Omega^2$ model universally predicts at or above-target tip–speed ratios ($\lambda \geq \lambda$). This demonstrates a potential weakness with implementing the model based on

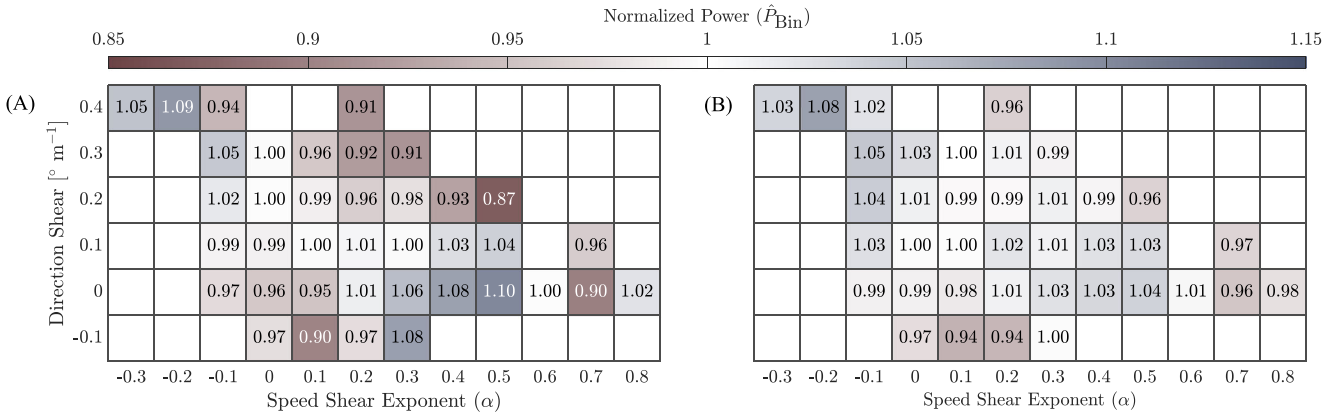

FIGURE 13 Bin averages of normalized power predictions ($\hat{P}_{\text{Bin}}$) for the BE model. Panel (A) shows the BE model outputs for Case 1 ($a = 1/3; \lambda_{\text{SCADA}}$), the model with the lowest overall error, and (B) the model predictions for Case 3 ($a = 1/3; \lambda^*$), the model setup that produces the lowest overall error when Ω is not taken from the SCADA data.

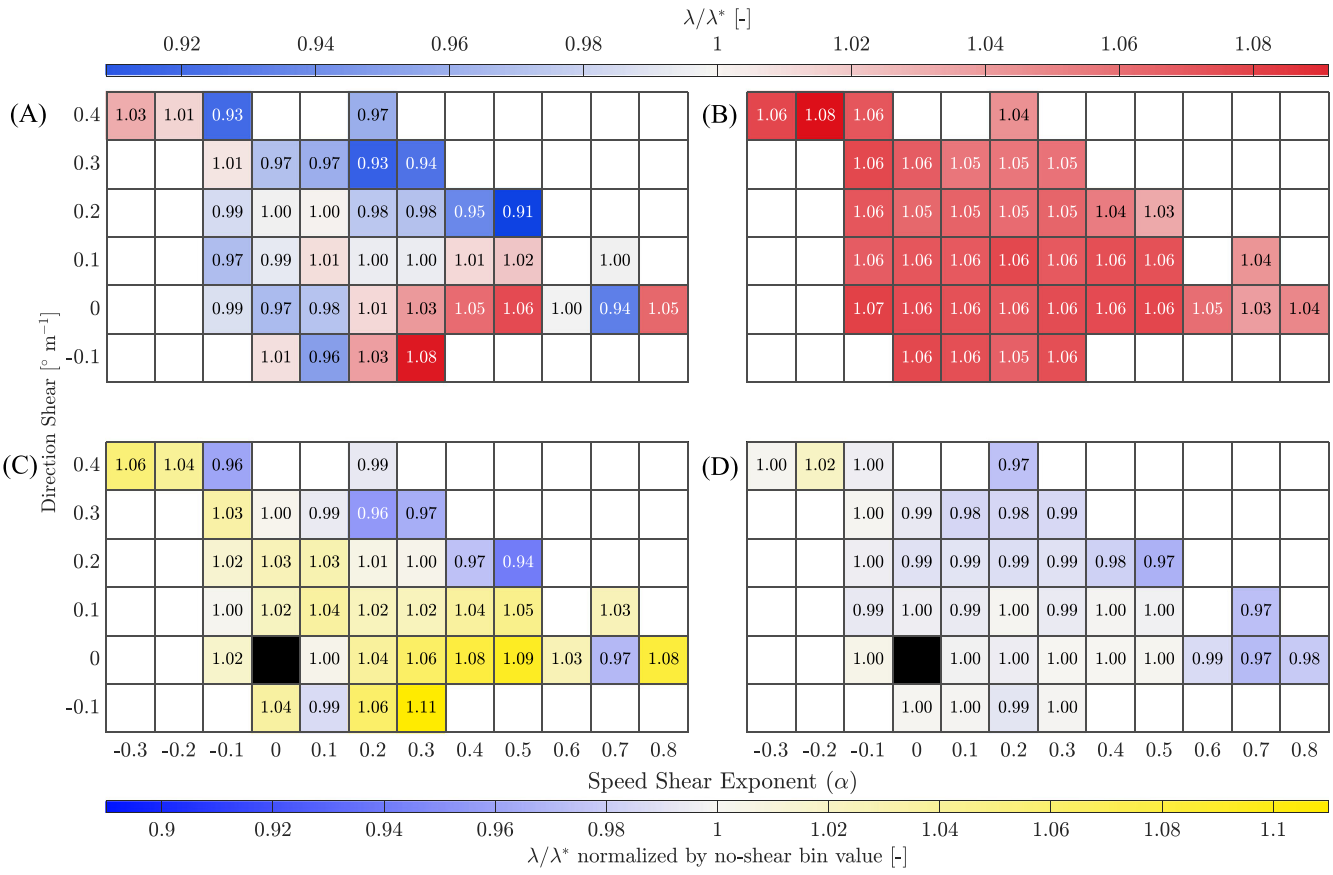

FIGURE 14 Panel (A) shows normalized values of the tip–speed ratio λ from the SCADA data. Panel (B) shows normalized values of the predicted tip–speed ratio λ from the BE model with constant ($a = 1/3$) induction closure and the $k - \Omega^2$ controller model (Case 2). All values are normalized with respect to the target tip–speed ratio in Region II (λ^*). Panel (C) shows the same information in (A) normalized by the bin value corresponding to no speed or direction shear (indicated by the black square). Similarly, panel (D) shows the same information in panel (B) normalized in the same fashion.

SCADA data. There are inherent differences between the true physical processes taking place at the turbine rotor and the BE model based on the simplifications and assumptions to the model detailed in this section. Imposing a value of k determined from the SCADA data in the BE model operates the turbine away from the true target tip–speed ratio in the field measurements, causing the values of λ/λ^* in Figure 14B to be

universally above 1. However, in an analysis where k was chosen to on average produce the target tip–speed ratio from the SCADA data λ^*, the variations in predicted λ (i.e., those in Figure 14D) remained unchanged.

5 | DISCUSSION AND FUTURE WORK

In this study, we analyze a set of LiDAR wind speed and direction measurements and SCADA power measurements to quantify the effect of shear on turbine power production. We observe distinct regions of over-performance and under-performance based on differing combinations of speed and direction shear. We relate these observations to a previous study of similar design[25] and note that different combinations of shear correspond to similar but distinct trends in turbine performance between the two studies. A potential cause of differences between the results of these two studies is the frequency of occurrence of LLJs at each site. As noted in Section 3.1, the power law used to characterize the degree of speed shear in both studies is not capable of modeling the complex wind speed profiles inherent to LLJs. Specifically, the power law cannot model wind speed profiles that do not increase or decrease monotonically with height. When the core of an LLJ descends into the turbine rotor area, there exists some degree of both positive and negative shear over the rotor, which the power law cannot characterize. This may increase the error between the power law fit and the true wind speed profile, which could shift data between bins in the plots shown in Figures 6–8, thereby changing the observed empirical trends in over-performance and under-performance.

Given these limitations in parsing the empirical trends based on the high-dimensional ABL flow, we focus on developing and assessing parametric models for the effect of wind shear on power production. We assess the predictions of three different models for turbine power production that account for wind speed and direction shear over the rotor area and compare these results to a model that has no knowledge of wind shear. We drive each model with two separate and distinct input classes: (1) best-fit canonical ABL profiles where wind speed is modeled with the power law and wind direction varies linearly with height and (2) wind speed and direction measurements made by a profiling LiDAR. These two input types are observed to produce qualitative and quantitative differences in power predictions in each model. These results indicate that the variations present in complex wind speed and direction profiles that are not present in median profiles have a first-order effect on model outputs. This implies that the model outputs may vary substantially as the frequency of the input wind conditions changes. That is, as the time-averaging window of the input wind profiles increases, for instance to 10 min, as is standard in industry wind resources assessments, the model predictions may vary from those produced by higher frequency inputs like those used in this study. Since power production is a nonlinear function of the wind speed, the average power production based on instantaneous wind is not equivalent to the power production based on the averaged wind, and there is therefore inherently a dependence on the time-averaging scale. Future work should further elucidate the time-averaging scale that is necessary to accurately model the influence of wind shear, since lowering the averaging period will also further complicate the qualitative characterization of the profiles as they become more sensitive to microscale ABL turbulence. Further, the present results have an implication on wind resource assessment: power predictions assuming power law profile behavior made in the absence of real wind profile measurements may deviate substantially from true values based on the assumptions made about the input wind profiles. Specifically, if canonical ABL profiles are used in which no short-term turbulent fluctuations or diurnally varying atmospheric features (such as LLJs) are accounted for, predictions of power may not accurately reflect the true power production at a given site.

We compare the predictions from each model driven with LiDAR wind speed and direction inputs to concurrent power measurements from a utility-scale wind turbine located adjacent to the LiDAR system. The hub height wind speed model has no knowledge of variations in wind speed and direction over the rotor and is included as a reference against which the other models that do have knowledge of variations over the rotor are compared. We assess the models in two separate ways. First, the model results are analyzed when power predictions are dominated by the wind speed magnitude in the input wind profile. Second, we isolate the effect of shear and other determinants of power by normalizing the power predictions by the aerodynamic power of the rotor based on the hub height wind speed of the input wind profile. In both cases, we observe that the BE model shows the highest correlation and lowest overall error with the SCADA measurements. The two rotor-equivalent models show similar correlations and overall errors in both cases. However, the correlations of the REWS and REP models to the SCADA measurements decrease by a factor of 2 when normalized to isolate the effect of shear, whereas the BE model correlation decreases only marginally. The implication of this is that the BE model is more able to accurately model the effect of speed and direction shear in arbitrary wind profile inputs on turbine power production than the rotor-equivalent models in their current form.

While the results presented in Figure 11 show promise in capturing the effects of wind shear with a BE approach, a notable weakness for this model is the additional information required, which is not necessary to drive the two rotor-equivalent models, namely, the airfoil properties corresponding to each blade node, as well as the rotor angular velocity corresponding to the atmospheric conditions in each input wind profile. Figure 13 demonstrates the degree to which knowledge of the angular velocity affects the BE model power predictions. When Ω is computed from the target tip–speed ratio of the turbine λ^*, the BE model accuracy decreases substantially. The correlation with SCADA power measurements when power is dominated by the cubic dependence of power on wind speed falls to $\mathcal{R} = 0.67$, and when the cubic dependence is accounted for, the correlation is $\mathcal{R} = 0.36$. With knowledge of Ω removed, in the best case, results are comparable to the two rotor-equivalent models and in the remaining cases under-perform even the hub height wind speed model. Moreover, Figure 14A shows that the average tip–

speed ratio for discrete combinations of speed and direction shear follows similar trends as the normalized power production shown in Figure 8. This suggests that the BE model depends on information pertaining to the specific operating strategy commanded by the onboard control system, and when this information is removed by assuming a constant tip–speed ratio for Region II operation, rather than known a priori, the BE model has similar performance to the actuator disc models considered. Therefore, future work on accurately estimating the tip–speed ratio depending on wind shear, and other atmospheric and wind turbine control determinants, is particularly pertinent.

Uncertainty exists around how rotor aerodynamics (e.g., induction factors) are affected by wind speed and direction shear. We test several simplifications and assumptions to demonstrate their effect on the BE model results. Elucidating how these aerodynamic mechanisms depend on wind speed and direction shear, and then incorporating any corresponding extensions developed into the BE framework proposed here, is suggested for future work. In a sensitivity test of the effect of induction closure and turbine control on the BE model results, we find that the model is dependent on knowledge of the rotor speed to first order. Further, when the tip–speed ratio is estimated using the standard controller model from the literature ($k - \Omega^2$), the predictions are under-dispersive relative to the measured SCADA values. This result holds regardless of the induction closure used; however, induction closure from one-dimensional momentum theory appears to further increase error relative to the measured SCADA data. This indicates that the momentum theory induction closure model has a stabilizing effect on the controller model, such that when both are used in tandem, feedback between the two models tends to mitigate the effect of arbitrary wind speed and direction shear on model outputs. Moreover, none of the cases tested in the sensitivity analysis were able to meet or exceed the benchmark correlation or error achieved by the BE model when run with constant induction closure and the SCADA tip–speed ratio. This again underscores the impact that knowledge of the tip–speed ratio has on the BE model predictions and denotes limitations in both the induction closure and controller models in handling inputs containing shear. Future work should focus on understanding how the induced velocities depend on wind speed and direction shear, and on estimating λ, and by extension Ω, based on the turbine controller response to inflow wind conditions. This will enable the BE model to be used for predictions where SCADA measurements of these quantities are not available (e.g., wind farm siting and design).

Finally, the BE model does not consider the effect of any other determinants of turbine efficiency, such as turbulence at scales smaller than the time-averaging timescale, which has been studied in empirical investigations and actuator disc formulations extensively (see, e.g., Wharton and Lundquist,[18,19] Murphy et al,[22] Brand et al,[56] Ryu et al,[3] and St. Martin et al[20]). While high-frequency turbulence measurements over the rotor area were not available in this study, future work may assess the potential joint role of shear and turbulence using meteorological tower measurements and computational fluid dynamics. In this study, the BE model demonstrates the lowest error in predicting power depending on wind shear when rotor speed is known from SCADA measurements, though performance degrades when rotor speed is estimated from BE momentum theory. The model that is found to most accurately predict turbine power production depending on wind speed and direction shear, without knowledge from SCADA measurements, across multiple wind farm sites should be incorporated into future wind resource assessments for wind farm siting and design.

AUTHOR CONTRIBUTIONS

Storm A. Mata: Investigation (lead); visualization (lead); writing—original draft preparation (lead); writing—review and editing (equal). **Michael F. Howland:** Conceptualization (lead); supervision (lead); writing—review and editing (equal). **Juan José Pena Martínez**, **Jesús Bas Quesada**, **Felipe Palou Larrañaga**, **Neeraj Yadav**, **Jasvipul S. Chawla**, and **Varun Sivaram**: Data collection and curation (equal).

ACKNOWLEDGEMENTS

S.A.M. gratefully acknowledges partial support from the MIT Office of the Vice Chancellor, the Gates Millennium Scholars Program, a Chevron Corporation scholarship, and the United States Department of Energy. M.F.H. gratefully acknowledges support from the National Science Foundation under Grant CBET 2226053 (Program Manager Ron Joslin) and partial support from Siemens Gamesa Renewable Energy.

This material is based upon work supported by the U.S. Department of Energy, Office of Science, Office of Advanced Scientific Computing Research, Department of Energy Computational Science Graduate Fellowship under Award Number DE-SC0023112.

This report was prepared as an account of work sponsored by an agency of the United States Government. Neither the United States Government nor any agency thereof, nor any of their employees, makes any warranty, express or implied, or assumes any legal liability or responsibility for the accuracy, completeness, or usefulness of any information, apparatus, product, or process disclosed, or represents that its use would not infringe privately owned rights. Reference herein to any specific commercial product, process, or service by trade name, trademark, manufacturer, or otherwise does not necessarily constitute or imply its endorsement, recommendation, or favoring by the United States Government or any agency thereof. The views and opinions of authors expressed herein do not necessarily state or reflect those of the United States Government or any agency thereof.

The authors thank Jaime Liew and Paul Hulsman for many productive discussions throughout the preparation of this report. The authors would also like to thank ReNew Power and Siemens Gamesa Renewable Energy for support throughout this study.

CONFLICT OF INTEREST STATEMENT

The authors declare no potential conflict of interests.

PEER REVIEW

The peer review history for this article is available at https://www.webofscience.com/api/gateway/wos/peer-review/10.1002/we.2917.

DATA AVAILABILITY STATEMENT

The data used in this study are confidential at the request of the wind farm operator.

ORCID

Storm A. Mata https://orcid.org/0000-0001-8910-6933
Jasvipul S. Chawla https://orcid.org/0000-0002-9129-7975

REFERENCES

1. Wiser R, Bolinger M, Hoen B, et al. Land-Based Wind Market Report: 2022 Edition. Rep. DOE/GO-102022-5763, U.S. Department of Energy, Office of Scientific and Technical Information; 2022. Online.
2. Musial W, Spitsen P, Duffy P, et al. Offshore Wind Market Report: 2022 Edition. Rep. DOE/GO-102022-5765, U.S. Department of Energy, Office of Scientific and Technical Information; 2022. Online.
3. Ryu GH, Kim D, Kim D-Y, et al. Analysis of vertical wind shear effects on offshore wind energy prediction accuracy applying rotor equivalent wind speed and the relationship with atmospheric stability. *Appl Sci*. 2022;12(14):6949. https://www.mdpi.com/2076-3417/12/14/6949
4. Veers P, Dykes K, Lantz E, et al. Grand challenges in the science of wind energy. *Science*. 2019;366(6464):eaau2027. https://doi.org/10.1126/science.aau2027
5. Markowski P, Richardson Y. On the classification of vertical wind shear as directional shear versus speed shear. *Weather Forecast*. 2006;21(2):242-247. https://journals.ametsoc.org/view/journals/wefo/21/2/waf897_1.xml
6. Lundquist JK. Wind shear and wind veer effects on wind turbines. In: Stoevesandt B, Schepers G, Fuglsang P, Yuping S, eds. *Handbook of Wind Energy Aerodynamics*: Springer International Publishing; 2020:1-22. https://doi.org/10.1007/978-3-030-05455-7_44-1
7. Stull RB. *An Introduction to Boundary Layer Meteorology*: Kluwer Academic Publishers; 1988;1-28.
8. Lange J, Mann J, Berg J, et al. For wind turbines in complex terrain, the devil is in the detail. *Environ Res Lett*. 2017;12(9):094020. https://doi.org/10.1088/1748-9326/aa81db
9. Liew J, Urbán AM, Andersen SJ. Analytical model for the power–yaw sensitivity of wind turbines operating in full wake. *Wind Energy Sci*. 2020;5(1):427-437. https://doi.org/10.5194/wes-5-427-2020
10. Wyngaard JC. *Turbulence in the Atmosphere*: Cambridge University Press; 2010;193-214.
11. Debnath M, Moriarty P, Krishnamurthy R, et al. Characterization of wind speed and directional shear at the AWAKEN field campaign site. *J Renew Sustain Energy*. 2023;15(3):033308. https://doi.org/10.1063/5.0139737
12. Walter K, Weiss CC, Swift AHP, Chapman J, Kelley ND. Speed and direction shear in the stable nocturnal boundary layer. *J Solar Energy Eng*. 2009;131(1):011013. https://doi.org/10.1115/1.3035818
13. Howland MF, Ghate AS, Quesada JB, et al. Optimal closed-loop wake steering—Part 2: diurnal cycle atmospheric boundary layer conditions. *Wind Energy Sci*. 2022;7(1):345-365. https://doi.org/10.5194/wes-7-345-2022
14. Van Ulden AP, Holtslag AAM. Estimation of atmospheric boundary layer parameters for diffusion applications. *J Appl Meteorol Climatol*. 1985;24(11):1196-1207. https://journals.ametsoc.org/view/journals/apme/24/11/1520-0450_1985_024_1196_eoablp_2_0_co_2.xml
15. Peña A, Floors R, Gryning S-E. The Høvsøre tall wind-profile experiment: a description of wind profile observations in the atmospheric boundary layer. *Bound-Layer Meteorol*. 2014;150(1):69-89.
16. Lindvall J, Svensson G. Wind turning in the atmospheric boundary layer over land. *Quart J Royal Meteorol Soc*. 2019;145(724):3074-3088. https://rmets.onlinelibrary.wiley.com/doi/abs/10.1002/qj.3605
17. Shu Z, Li Q, He Y, Chan PW. Investigation of marine wind veer characteristics using wind Lidar measurements. *Atmosphere*. 2020;11(11):1178. https://www.mdpi.com/2073-4433/11/11/1178
18. Wharton S, Lundquist JK. Assessing atmospheric stability and its impacts on rotor-disk wind characteristics at an onshore wind farm. *Wind Energy*. 2012;15(4):525-546. https://onlinelibrary.wiley.com/doi/abs/10.1002/we.483
19. Wharton S, Lundquist JK. Atmospheric stability affects wind turbine power collection. *Environ Res Lett*. 2012;7(1):014005. https://doi.org/10.1088/1748-9326/7/1/014005
20. St. Martin CM, Lundquist JK, Clifton A, Poulos GS, Schreck SJ. Wind turbine power production and annual energy production depend on atmospheric stability and turbulence. *Wind Energy Sci*. 2016;1(2):221-236. https://wes.copernicus.org/articles/1/221/2016/
21. Vanderwende BJ, Lundquist JK. The modification of wind turbine performance by statistically distinct atmospheric regimes. *Environ Res Lett*. 2012;7(3):034035. https://doi.org/10.1088/1748-9326/7/3/034035
22. Murphy P, Lundquist JK, Fleming P. How wind speed shear and directional veer affect the power production of a megawatt-scale operational wind turbine. *Wind Energy Sci*. 2020;5(3):1169-1190. https://wes.copernicus.org/articles/5/1169/2020/
23. Howland MF, Moral Gonzlez C, Pena Martnez JJ, et al. Influence of atmospheric conditions on the power production of utility-scale wind turbines in yaw misalignment. *J Renew Sustain Energy*. 2020;12(6):063307. https://doi.org/10.1063/5.0023746
24. Howland MF, Quesada JB, Martínez JJP, et al. Collective wind farm operation based on a predictive model increases utility-scale energy production. *Nature Energy*. 2022;7(9):818-827. https://doi.org/10.1038/s41560-022-01085-8
25. Sanchez Gomez M, Lundquist JK. The effect of wind direction shear on turbine performance in a wind farm in central Iowa. *Wind Energy Sci*. 2020;5(1):125-139. https://wes.copernicus.org/articles/5/125/2020/
26. Manwell JF, McGowan JG. Wind characteristics and resources. *Wind Energy Explained*: John Wiley & Sons, Ltd; 2009:23-90.
27. Lydia M, Selvakumar AI, Kumar SS, Prem Kumar GE. Advanced algorithms for wind turbine power curve modeling. *IEEE Trans Sustain Energy*. 2013;4(3):827-835. https://doi.org/10.1109/TSTE.2013.2247641

28. Lydia M, Kumar SS, Selvakumar AI, Prem Kumar GE. A comprehensive review on wind turbine power curve modeling techniques. *Renew Sustain Energy Rev*. 2014;30:452-460. https://www.sciencedirect.com/science/article/pii/S1364032113007296
29. Wagner R, Antoniou I, Pedersen SM, Courtney MS, Jrgensen HE. The influence of the wind speed profile on wind turbine performance measurements. *Wind Energy*. 2009;12(4):348-362. https://onlinelibrary.wiley.com/doi/abs/10.1002/we.297
30. Choukulkar A, Pichugina Y, Clack CTM, et al. A new formulation for rotor equivalent wind speed for wind resource assessment and wind power forecasting. *Wind Energy*. 2016;19(8):1439-1452. https://onlinelibrary.wiley.com/doi/abs/10.1002/we.1929
31. Wagner R, Courtney MS, Gottschall J, Lindelöw PJP. Accounting for the speed shear in wind turbine power performance measurement. *Wind Energy*. 2011;14(8):993-1004. https://doi.org/10.1002/we.509
32. Clack CTM, Alexander A, Choukulkar A, MacDonald AE. Demonstrating the effect of vertical and directional shear for resource mapping of wind power. *Wind Energy*. 2016;19(9):1687-1697. https://onlinelibrary.wiley.com/doi/abs/10.1002/we.1944
33. Redfern S, Olson JB, Lundquist JK, Clack CTM. Incorporation of the rotor-equivalent wind speed into the weather research and forecasting model's wind farm parameterization. *Monthly Weather Rev*. 2019;147(3):1029-1046. https://journals.ametsoc.org/view/journals/mwre/147/3/mwr-d-18-0194.1.xml
34. Branlard E. Blade element theory (BET). In: Peinke J, van Bussel G, eds. *Wind Turbine Aerodynamics and Vorticity-Based Methods: Fundamentals and Recent Applications*: Springer International Publishing AG; 2017:143-150.
35. Weick FE. The simple blade-element theory. *Aircraft Propeller Design*: McGraw-Hill Book Company; 1930:37-50.
36. Kragh KA, Hansen MH. Load alleviation of wind turbines by yaw misalignment. *Wind Energy*. 2014;17(7):971-982. https://onlinelibrary.wiley.com/doi/abs/10.1002/we.1612
37. Madsen HA, Larsen TJ, Pirrung GR, Li A, Zahle F. Implementation of the blade element momentum model on a polar grid and its aeroelastic load impact. *Wind Energy Sci*. 2020;5(1):1-27. https://wes.copernicus.org/articles/5/1/2020/
38. Burton T, Sharpe D, Jenkins N, Bossanyi E. Aerodynamics of horizontal-axis wind turbines. *Wind Energy Handbook*: John Wiley & Sons, Ltd; 2001:41-172.
39. Branlard E. The blade element momentum (BEM) method. In: Peinke J, van Bussel G, eds. *Wind Turbine Aerodynamics and Vorticity-Based Methods: Fundamentals and Recent Applications*: Springer International Publishing AG; 2017:181-214.
40. Burton T, Jenkins N, Sharpe D, Bossanyi E. Aerodynamics of horizontal axis wind turbines. *Wind Energy Handbook*. 2nd ed.: John Wiley & Sons, Ltd; 2011:39-136.
41. Buhl M. A New Empirical Relationship Between Thrust Coefficient and Induction Factor for the Turbulent Windmill State. Rep. NREL/TP-500-36834,- National Renewable Energy Laboratory; 2005. Online.
42. Akhmatov V. Influence of wind direction on intense power fluctuations in large offshore windfarms in the North Sea. *Wind Eng*. 2007;31(1):59-64. https://doi.org/10.1260/030952407780811384
43. Lindelöw PJP. *UpWind D1. Uncertainties in wind assessment with lidar*: Danmarks Tekniske Universitet, RisøNationallaboratoriet for Bæredygtig Energi; 2009. Online.
44. WindCube: The Industry Standard Lidar for Accurate, Bankable Wind Data. B211897EN-G, Vaisala Inc; 2024.
45. Stull RB. *An Introduction to Boundary Layer Meteorology*: Kluwer Academic Publishers; 1988;75-114.
46. Wyngaard JC. *Turbulence in the Atmosphere*: Cambridge University Press; 2010;75-88.
47. Emeis S, Türk M. Comparison of logarithmic wind profiles and power law wind profiles and their applicability for offshore wind profiles. In: Peinke J, Schaumann P, Barth S, eds. *Wind Energy*, Proceedings of the Euromech Colloquium: Springer Science+Business Media; 2007:61-64. https://doi.org/10.1007/978-3-540-33866-6_11
48. Sanchez Gomez M, Lundquist JK. The effects of wind veer during the morning and evening transitions. *J Phys: Confer Ser*. 2020;1452(1):012075. https://doi.org/10.1088/1742-6596/1452/1/012075
49. Englberger A, Lundquist JK, Dörnbrack A. Changing the rotational direction of a wind turbine under veering inflow: a parameter study. *Wind Energy Sci*. 2020;5(4):1623-1644. https://wes.copernicus.org/articles/5/1623/2020/
50. Brugger P, Fuertes FC, Vahidzadeh M, Markfort CD, Portgel F. Characterization of wind turbine wakes with nacelle-mounted Doppler lidars and model validation in the presence of wind veer. *Remote Sens*. 2019;11(19):2247. https://www.mdpi.com/2072-4292/11/19/2247
51. Aird JA, Barthelmie RJ, Shepherd TJ, Pryor SC. WRF-simulated low-level jets over Iowa: characterization and sensitivity studies. *Wind Energy Science*. 2021;6(4):1015-1030. https://wes.copernicus.org/articles/6/1015/2021/
52. Kalverla PC, Duncan Jr. JB, Steeneveld G-J, Holtslag AAM. Low-level jets over the North Sea based on ERA5 and observations: together they do better. *Wind Energy Science*. 2019;4(2):193-209. https://wes.copernicus.org/articles/4/193/2019/
53. Weide Luiz E, Fiedler S. Spatiotemporal observations of nocturnal low-level jets and impacts on wind power production. *Wind Energy Science*. 2022;7(4):1575-1591. https://wes.copernicus.org/articles/7/1575/2022/
54. Stull RB. *An Introduction to Boundary Layer Meteorology*: Kluwer Academic Publishers; 1988;197-250.
55. Walter KR. Wind Power Systems in the Stable Nocturnal Boundary Layer. *Dissertation*; 2007.
56. Brand AJ, Peinke J, Mann J. Turbulence and wind turbines. *J Phys: Confer Ser*. 2011;318(7):072005. https://doi.org/10.1088/1742-6596/318/7/072005

How to cite this article: Mata SA, Pena Martínez JJ, Bas Quesada J, et al. Modeling the effect of wind speed and direction shear on utility-scale wind turbine power production. *Wind Energy*. 2024;1-27. doi:10.1002/we.2917

APPENDIX A: THE STATISTICAL SIGNIFICANCE OF POWER PREDICTIONS

To determine the statistical significance of the trends in over-performance and under-performance in the empirical results and model predictions, we perform the following analysis. The 95% confidence interval (CI) is computed around the mean value of each bin shown in Figure 8 using bootstrapping. In Figure A1, we remove the bins in which the CI contains the value of normalized power equal to one ($\hat{P}_{\text{Bin}} = 1$). These bins are removed because the CI crosses the threshold of over-performance and under-performance, indicating that at the selected 95% significance level, the performance reflected in these bins is not statistically significant.

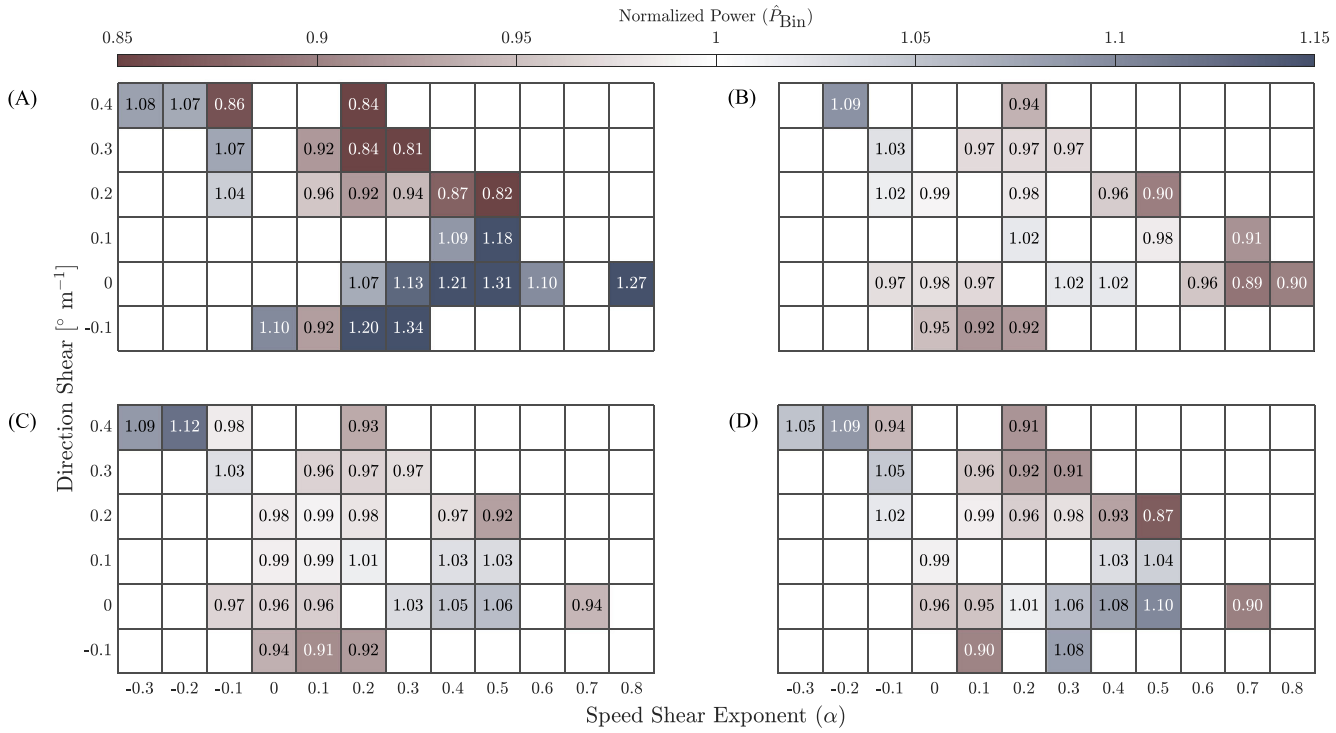

FIGURE A1 Bin averages of normalized power ($\hat{P}_{\text{Bin}}$) with respect to the median power curve of the turbine at the site for discrete combinations of speed and direction shear. Panel (A) shows the SCADA power measurements. Panel (B) shows the REWS model predictions, (C) the REP model, and (D) the BE model from LiDAR wind profile inputs. The colormap is chosen to highlight trends in the model predictions presented in (B)–(D). The 95% confidence interval (CI) is computed for each bin. Bins for which the CI spans the value of $\hat{P}_{\text{Bin}} = 1$ are removed because trends in over-performance and under-performance indicated in these bins cannot be discerned reliably with the given data.